



ICQNM 2018

The Twelfth International Conference on Quantum, Nano/Bio, and Micro
Technologies

ISBN: 978-1-61208-665-1

September 16 - 20, 2018

Venice, Italy

ICQNM 2018 Editors

Daniel Dundas, School of Mathematics, Queens' University, Belfast, UK

Anne Hémerlyck, LAAS-CNRS, Toulouse, France

Eric Surraud, University Paul Sabatier, Toulouse, France

ICQNM 2018

Forward

The Twelfth International Conference on Quantum, Nano/Bio, and Micro Technologies (ICQNM 2018), held between September 16, 2018 and September 20, 2018 in Venice, Italy, continued a series of events covering particularly promising theories and technologies. The conference covered fundamentals on designing, implementing, testing, validating and maintaining various kinds of materials, systems, techniques and mechanisms related to quantum-, nano- and micro-technologies.

Quantum technologies and nano technologies have a great potential to transform communications telecommunications infrastructure and communication protocols, and computers and networking devices. Nanotechnologies and micro-technologies already made their mark on smart materials, nano-medicine, nano-devices, molecular manufacturing, biotechnology, metrology, aerospace.

The advancements in material science and computer science have allowed the building, launching and deploying of space exploration systems that continually do more and more as they become smaller and lighter. As an example, carbon nano-tubes have been created that are 250 times stronger than steel, 10 times lighter, and transparent. Similar advances are occurring in glass, plastics and concrete. Spacecraft are being launched, with hulls that are composed of carbon fibers, a light weight high strength material.

Swarms is another concept of nano-robotics; swarms act in unison like bees. They theoretically will act as a flexible cloth like material, as strong as diamond. Interplanetary exploration can be foreseen as being carried on by nano-robots as well.

Electronic devices, medicine, environment, metrology, aerospace programs, clothes and materials, telecommunications, cryptography, semiconductors, manufacturing, and other domains are impacted by the progress on the areas mentioned above. Particularly, micro imaging, nano-medicine: (drug delivery; nano-particles i.e. viruses; proteins.), bio-nanostructures: (nano-tubes, nano-particles), microsystems, micro fluidics: (including nano-fluidics, modeling; fabrication and application), micro instrumentation / implantable microdevices (miniaturized bio-electronic systems etc.) and micro sensors benefits from the progress on quantum, nano and micro technologies.

We take here the opportunity to warmly thank all the members of the ICQNM 2018 technical program committee, as well as all the reviewers. The creation of such a high quality conference program would not have been possible without their involvement. We also kindly thank all the authors who dedicated their time and effort to contribute to ICQNM 2018. We truly believe that, thanks to all these efforts, the final conference program consisted of top quality contributions.

We also gratefully thank the members of the ICQNM 2018 organizing committee for their help in handling the logistics and for their work that made this professional meeting a success.

We hope that ICQNM 2018 was a successful international forum for the exchange of ideas and results between academia and industry and to promote further progress in the field of

quantum, nano/bio, and micro technologies. We also hope that Venice, Italy provided a pleasant environment during the conference and everyone saved some time to enjoy the unique charm of the city.

ICQNM 2018 Chairs

ICQNM Steering Committee

Sergey Yurish, IFSA, Spain

Shaya Fainman, University of California, San Diego, USA

Stefano Mancini, University of Camerino, Italy

Ashok Srivastava, Louisiana State University, Baton Rouge, USA

Vladimir Privman, Clarkson University - Potsdam, USA

Xin-Wei Yao, Zhejiang University of Technology, China

Masahito Hayashi, Nagoya University, Japan

ICQNM Research/Industry Committee

Thierry Ferrus, Hitachi Cambridge Laboratory, UK

Travis S. Humble, Oak Ridge National Laboratory, USA

Donald Sofge, Naval Research Laboratory, USA

Christian Kollmitzer, AIT Austrian Institute of Technology GmbH, Austria

Marco Genovese, Italian Metrological Institute (INRIM) -Torino, Italy

Keiji Matsumoto, National Institute of Informatics, Japan

ICQNM 2018 Committee

ICQNM Steering Committee

Sergey Yurish, IFSA, Spain

Shaya Fainman, University of California, San Diego, USA

Stefano Mancini, University of Camerino, Italy

Ashok Srivastava, Louisiana State University, Baton Rouge, USA

Vladimir Privman, Clarkson University - Potsdam, USA

Xin-Wei Yao, Zhejiang University of Technology, China

Masahito Hayashi, Nagoya University, Japan

ICQNM Research/Industry Committee

Thierry Ferrus, Hitachi Cambridge Laboratory, UK

Travis S. Humble, Oak Ridge National Laboratory, USA

Donald Sofge, Naval Research Laboratory, USA

Christian Kollmitzer, AIT Austrian Institute of Technology GmbH, Austria

Marco Genovese, Italian Metrological Institute (INRIM) -Torino, Italy

Keiji Matsumoto, National Institute of Informatics, Japan

ICQNM 2018 Technical Program Committee

Qammer H. Abbasi, Texas A&M University at Qatar, Qatar

Hossein Aghababa, University of Tehran, Iran

Mohamed Atef, Assiut University, Egypt

Michael Taynnan Barros, IRC Government of Ireland | Telecommunications Software and Systems Group (TSSG) | Waterford Institute of Technology (WIT), Ireland

Sang H. Choi, NASA Langley Research Center, USA

Eugen Dedu, Univ. Bourgogne Franche-Comté / FEMTO-ST Institute / CNRS Montbéliard, France

Shaya Fainman, University of California, San Diego, USA

Thierry Ferrus, Hitachi Cambridge Laboratory, UK

Marco Genovese, Italian Metrological Institute (INRIM) -Torino, Italy

Olga Glukhova, Saratov State University, Russia

Young-Geun Han, Hanyang University, Korea

Masahito Hayashi, Nagoya University, Japan

Liangxing Hu, Nanyang Technological University, Singapore

Travis S. Humble, Oak Ridge National Laboratory, USA

Kourosh Kalantar-Zadeh, Centre for Advanced Electronics and Sensors (CADES) | RMIT University, Melbourne, Australia

Oliver Keszöcze, University of Bremen / German Research Center for Artificial Intelligence, Germany

Christian Kollmitzer, AIT Austrian Institute of Technology GmbH, Austria

Jun Li, Kansas State University, USA

Jianlin Liu, University of California, Riverside, USA

Jianjun Ma, Brown University, USA
Jorge Maestre Vidal, Complutense University of Madrid (UCM), Spain
Stefano Mancini, University of Camerino, Italy
Keiji Matsumoto, National Institute of Informatics, Japan
Jose Manuel Molina Lopez, Universidad Carlos III de Madrid, Spain
Mevludin Memedi, Örebro University, Sweden
Masaki Nakanishi, Yamagata University, Japan
Ki-Hwan Nam, Korea Basic Science Institute (KBSI), Korea
Hock Chun Ong, Chinese University of Hong Kong, Hong Kong
Victor Ovchinnikov, Aalto University, Finland
Telhat Ozdogan, Amasya University, Turkey
Kwangjin Park, Wonkwang University, South Korea
Salvatore Petralia, ADG Central R&D | STMicroelectronics, Italy
Vladimir Privman, Clarkson University - Potsdam, USA
Peter Schartner, University of Klagenfurt, Austria
Stefan Schauer, AIT Austrian Institute of Technology GmbH - Vienna, Austria
O.L. Shanmugasundaram, K.S.Rangasamy College of Technology, India
Maciej Sitarz , AGH University of Science and Technology, Poland
Donald Sofge, Naval Research Laboratory, USA
Sandro Sozzo, University of Leicester, UK
Ashok Srivastava, Louisiana State University, Baton Rouge, USA
Ivo Stachiv, Harbin Institute of Technology, Shenzhen China & Institute of Physics - Czech Academy of Sciences, Prague, Czech Republic
Eric Suraud, Université Paul Sabatier, France
Pramod K. Tiwari, Indian Institute of Technology (IIT) Patna, India
Salvador Elias Venegas-Andraca, Tecnológico de Monterrey, Mexico
Robert Wille, Institute for Integrated Circuits | Johannes Kepler University, Linz, Austria
Xin-Wei Yao, Zhejiang University of Technology, China
Sergey Yurish, IFSA, Spain
Katerina Zaharieva, Institute of Catalysis | Bulgarian Academy of Sciences, Bulgaria
Alexander Zhbanov, Gwangju Institute of Science and Technology (GIST), Republic of Korea

Copyright Information

For your reference, this is the text governing the copyright release for material published by IARIA.

The copyright release is a transfer of publication rights, which allows IARIA and its partners to drive the dissemination of the published material. This allows IARIA to give articles increased visibility via distribution, inclusion in libraries, and arrangements for submission to indexes.

I, the undersigned, declare that the article is original, and that I represent the authors of this article in the copyright release matters. If this work has been done as work-for-hire, I have obtained all necessary clearances to execute a copyright release. I hereby irrevocably transfer exclusive copyright for this material to IARIA. I give IARIA permission to reproduce the work in any media format such as, but not limited to, print, digital, or electronic. I give IARIA permission to distribute the materials without restriction to any institutions or individuals. I give IARIA permission to submit the work for inclusion in article repositories as IARIA sees fit.

I, the undersigned, declare that to the best of my knowledge, the article does not contain libelous or otherwise unlawful contents or invading the right of privacy or infringing on a proprietary right.

Following the copyright release, any circulated version of the article must bear the copyright notice and any header and footer information that IARIA applies to the published article.

IARIA grants royalty-free permission to the authors to disseminate the work, under the above provisions, for any academic, commercial, or industrial use. IARIA grants royalty-free permission to any individuals or institutions to make the article available electronically, online, or in print.

IARIA acknowledges that rights to any algorithm, process, procedure, apparatus, or articles of manufacture remain with the authors and their employers.

I, the undersigned, understand that IARIA will not be liable, in contract, tort (including, without limitation, negligence), pre-contract or other representations (other than fraudulent misrepresentations) or otherwise in connection with the publication of my work.

Exception to the above is made for work-for-hire performed while employed by the government. In that case, copyright to the material remains with the said government. The rightful owners (authors and government entity) grant unlimited and unrestricted permission to IARIA, IARIA's contractors, and IARIA's partners to further distribute the work.

Table of Contents

A New Parallel Adaptive DSMC Algorithm for Unsteady Flows in Complex Geometries 1
Mirvat Shamseddine and Issam Lakkis

Brain Tumor Detection and Segmentation Using Hybrid Approach of MRI, DWT and K-Means 7
Parvinder Singh and Mansi Lather

A Phenomenological Model of Energy Relaxation in Disordered Insulators Irradiated by Ultrafast Proton Pulses 13
Lorenzo Stella, Jonathan Smyth, and Brendan Dromey

Ultrafast Photoionization and Energy Absorption in Bulk Silicon and Germanium 17
Tzveta Apostolova and Boyan Obreshkov

A New Parallel Adaptive DSMC Algorithm for Unsteady Flows in Complex Geometries

Mirvat Shamseddine, Issam Lakkis

Department of Mechanical Engineering
American University of Beirut, AUB

Email: mos05@mail.aub.edu, ilakkis@gmail.com

Abstract—We present an efficient parallel multi-scale Direct Simulation Monte Carlo (DSMC) algorithm for the simulation of three-dimensional unsteady rarefied gas flows over complex geometries. The flow domain is represented by a hierarchical octree-based Cartesian grid where three-dimensional solid objects with triangulated surfaces are incorporated using a cut-cell algorithm. The hierarchical octree domain representation allows the method to provide straightforward and efficient data management suitable for a particle-tracing and dynamic grid refinement and coarsening. The algorithm implements a spatial adaptivity scheme that is based on the gradients of statistically averaged macro-properties of the flow. The proposed DSMC algorithm employs a novel parallelization scheme suitable for simulating strongly unsteady, non-equilibrium flows. The parallelization scheme, implemented using Open Multi-Processing (OpenMP) for multicore Central Processing Units (CPUs), significantly reduces the computational cost of modeling these flows. The proposed DSMC algorithm is assessed for two fundamental flows in the slip and transition-continuum regimes.

Keywords—DSMC; Octree hierarchical grid; Spatially adaptive; Parallel; Rarefied gas flow; Ray tracing; Unsteady; Complex geometry.

I. INTRODUCTION

Rapid developments in micro and nano-technologies call for computational tools that efficiently and accurately predict the flow dynamics at these scales. The Direct Simulation Monte Carlo (DSMC) method has become the most widely used computational tool for simulating rarefied gas flows in the slip and transition regimes, characterized by the Knudsen number range $0.001 < \text{Kn} < 10$ [1]. Applications include investigation of the dynamics of the squeeze-film surrounding a microstructure undergoing oscillations of large amplitudes [2], investigation of the Knudsen thermal force on the performance of a low-pressure micro gas sensor [3], and prediction of rarefied flow fields in various micro/nano-systems [4], among others.

The geometry model in DSMC simulations refers to both the computational mesh and surface representation. Two primary approaches for the geometry model in existing state-of-the-art DSMC solvers include the unstructured body-fitted grids and the Cartesian-based grids. DSMC solvers can run with a single processor or in parallel using the Message Passing Interface (MPI) library on multiple processors. Parallelization is carried out by decomposition of the spatial domain among the processors. This flavor of parallelization suffers from two drawbacks. The first is the challenge of load balancing and distributed storage of the computational domain within a spatial-temporal adaptive algorithm that dynamically adjusts the computational grid and time step in response to the evolving flow field structures in unsteady flows. The second

challenge is that the criteria for spatial-temporal adaptivity are based on macroscopic properties computed as averages over a statistically meaningful number of realizations (a realization is a DSMC simulation initiated from a unique random number generator seed). This latter observation suggests parallelization over independent realizations. In the proposed framework, each thread or core processes a realization of the simulation of the unsteady flow over the entire computational domain.

In this paper, we present a three-dimensional DSMC algorithm parallelized over realizations, rendering it suitable for simulating unsteady flows. The flow domain is represented by a hybrid mesh consisting of a hierarchical octree-based Cartesian grid, whereas the surfaces of solid objects are represented by a triangular mesh. To allow for accurate DSMC simulations of flows over objects of complex boundaries, a cut-cell method is implemented [5]. The method, which calculates the volume of each flow cell cut by a solid boundary, enables accurate modeling of molecular collisions in these cells. The cut-cell method also allows for decoupling of the flow field mesh from the solid boundaries surface mesh, making it suitable for simulating near-continuum flows with large density variations. In addition, the method employs a dynamic spatial adaptation algorithm. The spatial adaptation criterion is based on the local macroscopic flow properties, which are computed as statistical averages over a number of realizations. The hierarchical octree-based Cartesian grid representation of the domain allows for an efficient data storage and management that is compatible with the spatial adaptation algorithm. Such representation significantly improves memory requirement when compared to unstructured meshes and, as such, is more suitable for simulating large-scale DSMC problems. It also enables a potentially more general scheme for varying cell volumes over a large range of the molecular length scales. The hybrid mesh scheme enables simple integration of a variety of effective geometric tools used in computer graphics, including fast particle-tracing algorithms. The scheme also enables spatial grid adaptation, molecular movement, and resorting to be performed with fewer operations. A key feature of the DSMC algorithm proposed in this work is that it is optimized for simulating unsteady flows in parallel over multiple cores. In contrast with distributing the domain over the cores, the independent realizations are distributed over the cores. Due to the lack of communication between the cores when each is handling an independent realization, the parallelization efficiency is almost 100 %. In addition, this type of parallelization is optimal when simulating highly unsteady rarefied flows over complex geometries. These flows typically experience considerable variability in the spatial gradients of the macroscopic thermodynamics properties, and as such,

spatial adaptation is frequently carried out. With each core being assigned a DSMC realization, local flow properties at different time steps are collected simultaneously in parallel and averaged over the multicores for local mesh refinement.

This paper is organized as follows: Section 2 summarizes the DSMC methodology. Section 3 presents the three-dimensional unsteady parallel DSMC algorithm. Validation of our algorithm through benchmark DSMC simulations of the micro-channel Poiseuille flow and the slider bearing flow problem is presented in Section 4. The conclusion is presented in Section 5.

II. DSMC METHODOLOGY

DSMC, pioneered by G. A. Bird in the 1960s [6], is the most widely used particle-based simulation method for the study of rarefied gas flows. The DSMC method is described in detail in the monograph by Bird [6]. A brief summary of the method, highlighting key aspects relevant to the algorithm we are proposing in this work, is presented next.

Based on the well-developed kinetic theory of gases, DSMC is a stochastic particle method that computationally solves the non-linear Boltzmann equation by emulating the physics of a real gas. The microscopic behaviour of the gas is modeled by tracking thousands or millions of randomly selected simulated particles, each representing a large number of physical molecules or atoms. The DSMC algorithm involves four major processes: 1) moving the particles over a time step and model their interactions with boundaries, 2) indexing and tracking the particles within the grid of collision cells, 3) selecting particles for collision on a probabilistic basis and applying the appropriate collision model, and 4) sampling the macroscopic flow properties.

For the DSMC method to produce physically realistic and accurate solutions, the time step, and grid cell size must be chosen as follows. The collision grid cell size, Δx , must be small compared to the local mean free path, $\lambda \sim |\pi/\nabla\pi|$; the length scale characterizing the spatial variations of the macroscopic properties, λ . So, we choose $\Delta x \ll \lambda$, where λ generally varies with space and time. The simulation time step Δt over which molecular motions and collisions are uncoupled must be smaller than the local mean collision time, $\Delta t < \tau_c = \lambda/V_{MP}$, where V_{MP} is the most probable velocity. In order to preserve collision statistics and to yield a reasonable approximation of the local velocity distribution function, the number of simulated gas molecules per cubic mean free path, N , must be larger than a minimum (typically 20).

In DSMC, simulated molecules move, collide with each other and with the physical boundaries. Different types of boundary conditions are employed in DSMC simulations. These include solid wall boundary conditions (thermal walls and periodic boundaries), and inflow/outflow boundary conditions. The interaction between a gas molecule and a solid boundary can be treated as being fully specular, fully diffuse, or a combination of the two. The inflow/outflow boundary conditions can accommodate supersonic and subsonic flows. They are implemented by injecting particles into the computational domain at the external flow conditions. The inflow/outflow boundary conditions can be implemented in DSMC using the standard method or the reservoir method. The standard method involves a particle emission surface set at the flow boundary [6]. The well-known Maxwellian Reservoir Method

employs ghost cells at the boundaries of the DSMC computational domain that act as sinks and sources of the simulation particles [7]. The velocity of the molecules entering the flow field is generated according to the velocity distribution of the external flow.

After completing molecular movements, intermolecular collisions are simulated probabilistically using molecular collision models. Several collision models, designed to reproduce the real flow macroscopic behaviour, were applied successfully within the framework of DSMC. These models include the inverse power law model, the hard sphere (HS) model, the variable hard sphere model (VHS), and the variable soft sphere (VSS) model [6]. In the VSS model, the mean free path is given as:

$$\lambda_{VSS} = \frac{4\alpha(7-2\omega)(5-2\omega)}{5(\alpha+1)(\alpha+2)} \left(\frac{\mu}{n}\right) (2\pi m k_B T)^{-1/2} \quad (1)$$

$$\mu = \mu_{ref} \left(\frac{T}{T_{ref}}\right)^\omega$$

where m is the molecular mass, $n = \rho/m$ is the number density, μ_{ref} is the viscosity at reference temperature, and α is the scattering parameter ($\alpha = 1$ for VHS model). The viscosity index ω is related to the power exponent η in the inverse power law model as $\omega = \frac{1}{2} \frac{\eta+3}{\eta+1}$. In the HS model, the mean free path is expressed as:

$$\lambda_{HS} = \frac{1}{\sqrt{2}\pi d^2 n} \quad (2)$$

where d is the molecular diameter.

The DSMC method is an explicit time marching simulation algorithm. As such, it always produces unsteady flow simulations. The statistical scatter of DSMC computation varies according to the inverse square root of the sample size. Figure 1 illustrates two sampling methods used in DSMC: the steady and the unsteady sampling techniques. For predicting a steady flow field, a time average over a number of time steps is required to obtain smooth results. In this case, averaging must be carried out after the transient phase elapses and a steady behaviour is established. For simulating unsteady flows, ensemble-averaging is performed where the entire flow evolution is calculated repeatedly. The flow field is sampled at the appropriate flow sampling time steps. To compute the flow fields of the macroscopic thermodynamic properties, the samples are averaged over a sufficiently large number of flow realizations, each originating from a different random number generator seed.

III. THREE-DIMENSIONAL UNSTEADY DSMC ALGORITHM

In the current study, an octree-based Cartesian grid divides the computational domain into cubic cells, whereas the surface of the 3D solid object is triangulated using the preprocessing open-source software SALOME 7.5.1 [9]. Tree-based methods with the simple Cartesian structure and embedded hierarchy make use of recursive encoding schemes. These schemes render processes such as mesh adaptation, rebuilding, data access, and handling of fluid-solid interaction both simple and efficient.

Each solid object is bounded by a rectangular box. An axis-aligned box-box intersection test [10] is then carried out to identify collision cells neighbors and all cubic cells that

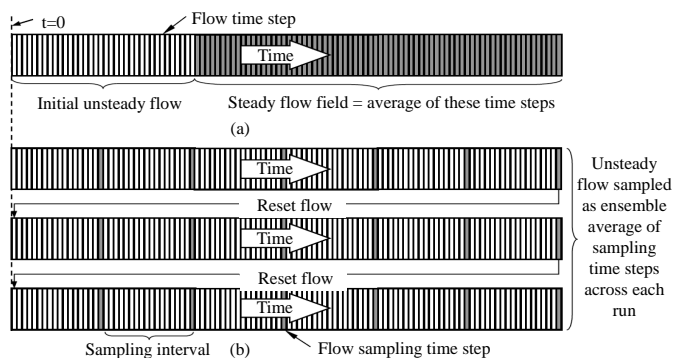


Figure 1. (a) The schematic of the time-averaging of the flow properties over a long interval of simulation time. (b) The schematic of the ensemble-averaging of the flow properties over many runs [8].

overlap with the bounding box surface. In addition, the fast 3D triangle-box overlap test by Moller [11] is implemented to test overlapping between triangular elements of the solid object surface mesh and cubic cells inside the bounding box. This test enables linking each surface mesh triangular element to the overlapping Cartesian cells. Figure 2(a) shows a schematic diagram illustrating the hybrid mesh scheme. Figure 2(b) shows a zoomed-in view of the box bounding the solid object (sphere). It also shows the cut-cell representation, where triangular solid surface elements cut the cubic cells in the adaptively refined Cartesian mesh. The resulting cut-cell volume is estimated using the Monte Carlo technique described in [5]. This volume is needed to accurately model collisions and predicts the macroscopic properties in the cut-cell. The proposed three-dimensional hybrid mesh scheme employs a flexible data structure which enables simulation of particles movement and sorting processes with fewer operations, thereby reducing the CPU time.

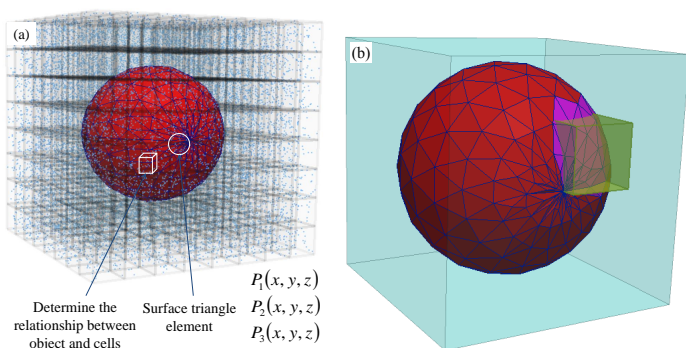


Figure 2. (a) Schematic representation of a triangulated surface mesh of a sphere embedded in a 3D octree Cartesian grid. (b) Bounding box and a cut-cell representation.

In the presence of complex solid boundaries (and/or when the surface to volume ratio of the flow domain is large), the computational cost of molecular movement amounts to a significant fraction of the computational cost of a DSMC simulation. To efficiently track the particle movement within the hierarchical octree-based Cartesian grid, a special particle ray-tracing technique is employed. This technique is used in the vicinity of the solid object surface where the region

of the bounding box is treated as follows. During a single time step, a molecule cannot move more than one collision cell size along each dimension (a DSMC time constraint). Ray tracing is performed only for particles that leave their assigned cell and intersect the box bounding the solid object. If an intersection with the bounding box occurs, a cell-by-cell particle tracking procedure is performed to determine whether the particle reaches a boundary surface triangle, stays in or leaves the current cell. If no ray-triangle intersection occurs, the particle's position is updated if the particle stays in the current cell; otherwise, ray-box intersection tests with all possible neighbour collision cells are performed to track the particle from the current cell to its nearest neighbour collision cell. The particle-tracking algorithm is then invoked again to move the particle over the remainder of the time step. At the completion of the molecular movement phase, each particle is automatically stored within its final cell by the sort subroutine. In summary, the hierarchical octree-based data structure allows for efficient intersection testing within the ray tracing algorithm. We point out here that the grid cells are axis-aligned boxes whose edges are all parallel to the basis vector, which enhances the efficiency.

Another special feature of the proposed algorithm is that it runs transient parallel Monte Carlo simulations simultaneously and independently on multicore CPUs. Figure 3 shows a schematic representation of the parallel algorithm using multiple cores. Each simulation consists of m transient solutions with n realizations each. Most DSMC solvers are parallelized through decomposition of the physical domain into groups of cells that are distributed among the processors. The efficiency of such parallelization scheme may suffer due to the intensive communications between the processors and load imbalance among the processors. In addition, this parallelization scheme is more convenient in simulating low speed flows where a uniform Cartesian grid is used and/or in simulating high-gradient flows where grid resolution in both space and time is evoked once before steady state is reached.

The proposed algorithm is also adaptive where refinement of the spatial grid is employed to simulate flows with length scales that vary considerably over the domain. Accurate prediction of these flows require variable resolution of different flow regions. Figure 4 shows the flow chart for the implemented DSMC method using the adaptive method. Prior to the adaptation process, the DSMC simulation starts with a uniform mesh. As depicted in the inset figure at the top right corner of Figure 3, periodic spatial adaptivity tests are carried out in the course of an unsteady simulation. The inset also shows the sampling times for predicting the transient macroscopic behaviour. Refinement or coarsening of collision grids is based on the averaged local flow variables over the multicores, which allows accurate prediction of these properties within a computationally efficient framework.

IV. BENCHMARK TEST CASES

To validate the proposed three-dimensional parallel DSMC algorithm, numerical simulations of two fundamental flows in the slip and transition-continuum regimes are presented. The Poiseuille flow is taken as an example to assess the spatial adaptation scheme in the slip flow regime. A three-dimensional flat slider gas bearing problem is considered to evaluate the hybrid mesh scheme in transition flow regime. The simulations

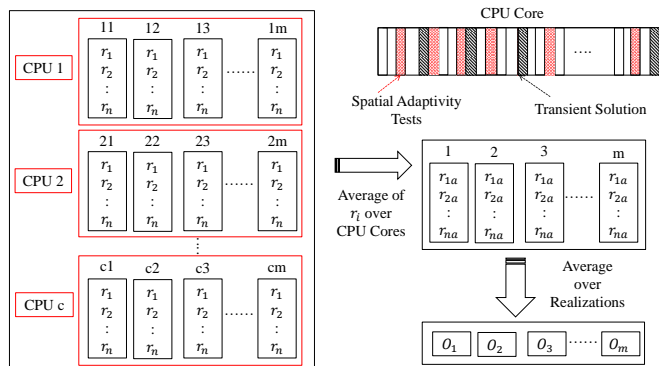


Figure 3. The schematic of running transient DSMC simulations on different CPU cores. The upper right figure displays the local adaptive and the flow sampling time steps.

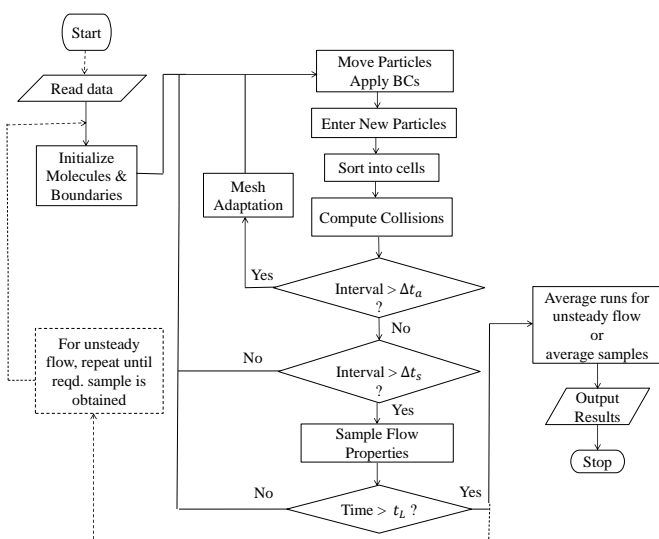


Figure 4. Simplified flow chart of the implemented DSMC algorithm. Δt_a : adaptive time; Δt_s : sampling time; t_L : Long time.

were carried out using Fortran in CentOS Linux 7 on 16 core Intel Xeon(R) CPU E5-2650 v2 running at 2.6 GHz.

A. Poiseuille Flow

The pressure-driven Poiseuille gas flow in a rectangular microchannel between two parallel plates is considered. The channel axis is along the x direction. The plates, of length L along the flow direction (x), are separated by a distance H , where $L/H \gg 1$. The flow is two dimensional in the $x - z$ plane; the channel dimension, W , along the y direction is much larger than H ; $W \gg H$. Since the flow is two dimensional in the $x - z$ plane, the computational domain consists of one grid cell in the y direction. The following boundary conditions were imposed: (i) solid-walls are assumed to be perfectly accommodating, (ii) periodic boundary conditions are enforced at the $x - z$ planes on either size of the domain, and (iii) the Maxwellian reservoir method is used for the inflow/outflow boundary conditions at the inlet and outlet of the channel. The simulated fluid is argon gas (VHS gas) initially at ambient conditions. The channel length is $L = 5 \mu m$, the channel aspect ratio is $L/H = 5$, the inlet flow stream temperature

is $T_{in} = 300 K$, the inlet to exit pressure ratio, $P_{in}/P_e = 3$, and the inlet pressure is $P_{in} = 160.839 kPa$. To assess the spatial adaptivity scheme in our DSMC algorithm, this flow is simulated with and without dynamic grid adaptation. For the non-adaptive simulation, the grid spacing was chosen to be $\Delta x \sim 1/5\lambda_0$, where λ_0 is the mean free path at the initial conditions. For the adaptive simulation, the grid spacing is computed as $\Delta x \sim \lambda/3$, where at each adaptation time interval, λ for each cell is computed using Eq. (1), where T and n for the cell are averaged over all the cores. Figure 5 shows the steady state centreline pressure distribution using the proposed DSMC algorithm with and without grid adaptation. Our results are in good agreement with the simulated pressure profile by Wu et al. [12], with the pressure profile predicted using the adaptive scheme closer to that predicted by Wu et al. [12]. The figure also shows the flow field refined mesh

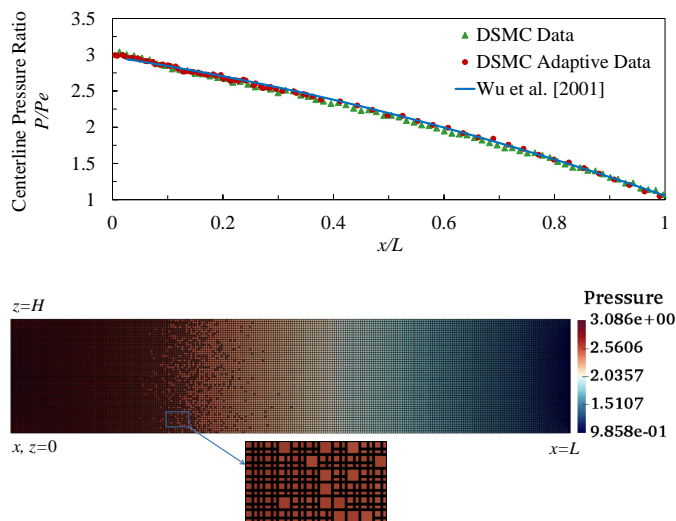


Figure 5. Centreline pressure distribution (top figure) and flow field refined mesh for a microchannel in the slip flow regime.

upon spatial adaptation where the size of an inlet collision cell is adapted to half the size of a collision cell at the exit; $\lambda_{in}/\lambda_e \sim P_{in}/P_e$. With $P_{in}/P_e = 3$ and since the octree divides a cell by integer powers of 2, λ_{in}/λ_e was set to 1/2.

The transient solution and spatial adaptivity sampling intervals are presented in Table I, among other parameters. The table also shows that at the end of the simulation, the number of cells in the adaptive simulation increased from 13056 to 48084, which is comparable to that used in the non-adaptive case. The computational cost of the adaptive simulation is, however, less by a factor of 7.7.

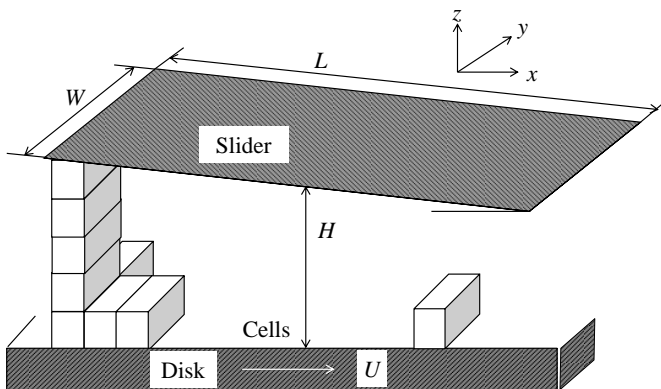
B. Slider Bearing Problem

Figure 6 shows a typical three-dimensional flat slider gas bearing configuration. A channel is formed by a moving horizontal bottom surface and a stationary slightly inclined surface whose length is $L = 5 \mu m$ and height at the trailing edge is $H_o = 50 nm$. The simulation used argon hard sphere particles initially at ambient conditions. Thus, the Knudsen number at the exit is $Kn_o = \lambda/H_o = 1.25$. The lower surface moving at a speed of $U = 25 m/s$ and the bearing number is $\Lambda = 61.6$ (defined as $\Lambda = 6\mu UL/p_a H_o^2$; p_a

TABLE I. COMPARISON OF ELAPSED TIME PER DSMC REALIZATION FOR NON-ADAPTIVE AND ADAPTIVE POISEUILLE FLOW.

	<i>Non-Adaptive</i>	<i>Adaptive</i>
Time step	14.48 ps	28.96 ps
Sampling time	55.3 ns	55.3 ns
Transient solution sampling interval	27.45 ns	27.45 ns
Spatial adaptivity sampling interval		18.299 ns
Total no. of time steps	3800	1900
Total Time per Realization per core	45910.5 s	5931.76 s
Initial no. of Cells	52224	13056
Final no. of Cells	52224	48084

is the ambient pressure and μ is the viscosity of the gas). As for the boundary condition, the solid-walls are assumed to be perfectly accommodating, periodic boundary conditions are enforced at the $x - z$ planes on either side of the 3D domain, and the Maxwellian reservoir method is used for the inflow/outflow boundary conditions at the inlet and outlet. Our


 Figure 6. Schematic of the slider bearing geometry, $L = 5\mu\text{m}$, $H_o = 5\mu\text{m}$, $U = 25\text{m/s}$.

DSMC results are in excellent agreement with the previously published DSMC solution by Garcia et al. [13].

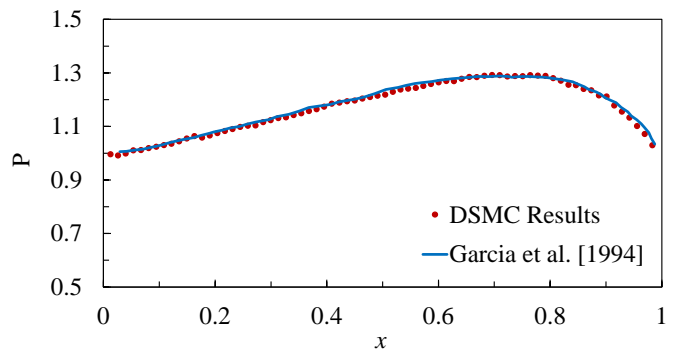
Table II shows the simulation time per time step per core distributed among the particles movement, sorting and collision time steps. It can be observed that the molecular motion in the slider bearing flow takes the longest time. This is due to the cost of the ray-tracing operations using the hybrid mesh constructed near the inclined surface.

TABLE II. ELAPSED TIME(S) OF DSMC PROCESSES AT FLOW SAMPLING TIME STEP FOR BENCHMARK SIMULATIONS.

	<i>Non-Adaptive Poiseuille</i>	<i>Adaptive Poiseuille</i>	<i>Slider Bearing</i>
Move Molecules	3.269	0.917	4.240
Sort Molecules	2.165	0.729	0.084
Perform Collisions	0.354	0.215	0.019

V. CONCLUSION

We presented a parallel three-dimensional DSMC algorithm to model rarefied gas flows in domains with complex solid boundaries. The algorithm employs a hierarchical octree-based Cartesian grid, accompanied by a cut-cell algorithm to incorporate complex 3D geometries with triangulated surfaces


 Figure 7. Slider bearing normalized pressure profile for $\text{Kn}_o = 1.25$, $\Lambda = 61.6$, $\text{Ma} = 0.08$.

within the grid cells. It also incorporates a multi-level spatial adaptivity scheme based on the macroscopic average of local flow properties. An original method of running parallel unsteady DSMC simulations simultaneously and independently on multicores is proposed. The selected geometry model is characterized by its low memory storage requirements compared to the use of non-Cartesian meshes, its ability to employ an efficient ray-tracing particle movement scheme, and its flexibility to enable a fully dynamic three-dimensional spatial adaptive scheme that maintains DSMC constraints consistent with the local variations of flow field properties. Correlation of computational results and experimental data clearly show the capability of the unsteady DSMC algorithm to provide accurate flow field predictions. In future work, we expect to complement the spatial adaptivity with a novel temporal adaptivity scheme and then showcase the efficiency and accuracy of the method in predicting unsteady flows in complex geometries encountered in micro- and nano-electromechanical systems (MEMS/NEMS).

REFERENCES

- [1] M. Gad-el Hak, "The fluid mechanics of microdevices—the Freeman scholar lecture," *Journal of Fluids Engineering*, vol. 121, no. 1, 1999, pp. 5–33.
- [2] N. A. Diab and I. A. Lakkis, "Investigation of the squeeze film dynamics underneath a microstructure with large oscillation amplitudes and inertia effects," *Journal of Tribology*, vol. 138, no. 3, 2016, p. 031704.
- [3] M. B. Gerdoozbary, D. Ganji, M. Taeibi-Rahni, and S. Vakili-pour, "Effect of Knudsen thermal force on the performance of low-pressure micro gas sensor," *The European Physical Journal Plus*, vol. 132, no. 7, 2017, p. 315.
- [4] E. Roohi, "DSMC simulations of nanoscale and microscale gas flow," in *Encyclopedia of Microfluidics and Nanofluidics*. Springer, 2015, pp. 681–693.
- [5] C. Zhang and T. E. Schwartzentruber, "Robust cut-cell algorithms for DSMC implementations employing multi-level Cartesian grids," *Computers & Fluids*, vol. 69, 2012, pp. 122–135.
- [6] G. A. Bird, *Molecular Gas Dynamics and the Direct Simulation of Gas Flows*. Clarendon Press, 1994, no. v. 1, 94003873.
- [7] M. W. Tysanner and A. L. Garcia, "Non-equilibrium behaviour of equilibrium reservoirs in molecular simulations," *International journal for numerical methods in fluids*, vol. 48, no. 12, 2005, pp. 1337–1349.
- [8] H. M. Cave et al., "Implementation of unsteady sampling procedures for the parallel direct simulation Monte Carlo method," *Journal of Computational Physics*, vol. 227, no. 12, 6/1 2008, pp. 6249–6271.

- [9] “CEA/DEN, EDF R&D and OPEN CASCADE, SALOME: the open source integration platform for numerical simulation,” 2015, URL: <https://www.salome-platform.org/> [accessed July 2018].
- [10] M. G. Coutinho, Guide to dynamic simulations of rigid bodies and particle systems. Springer Science & Business Media, 2012.
- [11] T. Akenine-Möller, “Fast 3D triangle-box overlap testing,” in ACM siggraph 2005 courses. ACM, 2005, p. 8.
- [12] J.-S. Wu and K.-C. Tseng, “Analysis of micro-scale gas flows with pressure boundaries using direct simulation Monte Carlo method,” *Computers & Fluids*, vol. 30, no. 6, 2001, pp. 711–735.
- [13] F. J. Alexander, A. L. Garcia, and B. J. Alder, “Direct simulation Monte Carlo for thin-film bearings,” *Physics of Fluids*, vol. 6, no. 12, 1994, pp. 3854–3860.

Brain Tumor Detection and Segmentation using Hybrid Approach of MRI, DWT and K-means

Parvinder Singh¹, Mansi Lather²

^{1,2}Department of Computer Science and Engineering

^{1,2}Deenbandhu Chhotu Ram University of Science and Technology, Murthal, Sonapat, India

¹parvindersingh.cse@dcrustm.org

²lathermansi@gmail.com

Abstract— In medical image processing, the detection of a brain tumor is considered as one of the most difficult and time consuming activities. The foremost aim of this paper is to design an efficient algorithm for brain tumor detection and segmentation. This paper presents an improved hybrid method using Discrete Wavelet Transform (DWT), morphological operators, K-means and Otsu's thresholding technique for detecting and segmenting the tumor in the brain. DWT is used for image denoising. Morphological operators are used for removing the skull portions from the brain images and K-means clustering and thresholding approaches are used for image segmentation and finally to detect the brain tumor. The proposed method results in low values of Mean Square Error (MSE) and Bit Error Rate (BER) and high value of Peak Signal to Noise Ratio (PSNR) as compared to existing watershed and region growing segmentation methods and thus outperforms the existing methods.

Keywords—Brain Tumor; Image Denoising; K-means Segmentation; Magnetic Resonance Imaging (MRI); Morphological Operators; Skull Removal.

I. INTRODUCTION

The brain is regarded as the command center of the nervous system, and it is the most complicated organ inside the human body. It is a non-replaceable, soft and spongy mass of tissue. The human brain takes inputs from the sensory organs and forwards them as outputs to the muscles [1]. Intelligence, creativity, emotions, memory, etc., are governed by the brain [2]. Therefore, any damage or harm in the brain will cause problems for personal health including mobility or cognition [1].

In diagnosing brain tumors, precise measurements are very difficult because of the diversity in size, shape and appearance of tumors. A brain tumor is an abnormal and uncontrolled propagation of cells [3]. A brain tumor does not only impact the immediate cells in its location, but it can also cause damage to surrounding cells by causing inflammation. In medical image processing, brain tumor detection is considered as one of the most difficult and time consuming activities [12]. Medical imaging techniques play an important role in tumor detection. Among the various medical imaging modalities, MRI is regarded as the most proficient means for analyzing the body's internal structure

[5]. Timely and precise tumor detection is necessary for efficiently planning the treatment. In this paper, we develop a hybrid technique for brain tumor detection using DWT, morphological operators and K-means segmentation.

The important goal of the image processing application proposed here is to use the image data to abstract the required attributes which are then used by a machine to obtain an interpretative, descriptive, or reasonable diagnosis.

Among the various image processing steps, in case of brain tumor detection, the main ones are image denoising, morphological operation and image segmentation.

Image denoising is defined as the method of removing noise from the image. In medical imaging, for easy and proper diagnosis of diseases, denoising produces a clearer image [5]. Various schemes are available for removing noise from images [4][14]. The selected diagnostic method should be capable of retrieving as much detail as possible from the image regardless of any high degradation of the image by noise. The image denoising methods are broadly categorized as [4]:

- **Spatial filtering methods**
Include linear and non-linear filters.
- **Transform domain filtering methods**
Include spatial frequency filtering methods and wavelet domain methods.

Morphological operators are non-linear operators dealing with morphology and shape of images. They are related to pixel ordering and they do not change the pixel's numerical value. These operators use a small matrix of pixels called structuring element in which each pixel has value one or zero and the choice of suitable structuring element plays an important role in the process. Various types of morphological operators include erosion, dilation, opening and closing [5].

Image segmentation is the process of using automatic or semi-automatic means of extracting the region of interest from an image [9]. Segmentation techniques used for analyzing medical images are classified as [6]:

- **Region based methods**
Include thresholding and region growing methods.
- **Classification methods**
Include k-nearest neighbor and maximum likelihood methods.

- **Clustering methods**

Include K-means, Fuzzy C-Means (FCM) and expectation maximization methods.

In this paper, we propose a new hybrid method using DWT, morphological operators, K-means and Otsu's thresholding technique for detecting and segmenting the tumor in the brain. Image denoising is done using DWT; The skull portion of the brain images is removed using morphological operators and image segmentation and final brain tumor detection is done using K-means clustering and thresholding.

This research paper is divided in five parts: in Section II, we present related literature works; in Section III, the proposed methodology is explained in detail; Section IV includes performance analysis and Section V concludes the paper.

II. LITERATURE REVIEW

In [5], *Ramya and Sasirekha* proposed a segmentation technique consisting of three phases: (1) a fourth order partial differential equation is used to denoise the image; then, (2) the morphological operators are used to remove the skull part and, finally, (3) segmentation is done using region growing segmentation. The precision of this method is higher than the watershed segmentation algorithm [5].

In [7], *Ayed, Halima and Kharrat* proposed an approach that consists of five stages: In the first stage, features are extracted using 2D Discrete Wavelet Transform and Spatial Gray Level Dependence Matrix (DWT-SGLDM). In the second stage, to reduce features size, features are selected using Simulated Annealing (SA). In the next stage, over fitting is avoided using Stratified K-fold Cross Validation. In the fourth stage, to optimize Support Vector Machine (SVM) parameters, Genetic Algorithm-SVM (GA-SVM) model is used. Finally SVM is used for creating the classifier.

In [8], *El-Khamy, El-Khoreby and Sadek* presented a hybrid approach of FCM and Conformed threshold. The proposed technique is composed of five steps: The first step involves enhancement of the intensity of input brain MR image using pre-processing for the next step. The second step involves the use of a rectangular window for image histogram in order to calculate the number of clusters for FCM input. The third step is to use FCM to find the center of clusters. The fourth step is to use the Conformed threshold value in order to segment the tumor. The final step uses segmented image to detect tumor. For correctness and processing time, this method gives better results than the global threshold method of segmentation, but the completeness is better in global threshold method as compared to their method.

In [10], *Gopal and Karnan* presented a hybrid approach such as FCM with GA and Particle Swarm Optimization (PSO) for detecting the tumor. The tumor detection is done in two phases. The first phase involves pre-processing and enhancement using the tracking algorithm to eliminate film artifacts and median filter to eliminate the high frequency components. The second phase involves segmentation and classification using GA with FCM and PSO with FCM.

PSO with FCM technique outperforms GA with FCM technique.

In [11], *Selkar and Thakare* presented watershed and thresholding algorithm that consists of three stages. Firstly, quality of the scanned image is enhanced by removing noise. Secondly, thresholding and watershed segmentation is applied to get a high intensity portion called tumor from the whole image. Finally, edge detection operator is applied for extracting the boundary and for finding the tumor size. The result shows efficient tumor detection by using thresholding algorithm rather than watershed algorithm and canny edge operator gives efficient boundary extraction results rather than Prewitt and Robert operator.

In [12], *Arivoli, Lakshmi and Vinupriyadharshini* proposed a system consisting of two main steps: preprocessing and segmentation. The preprocessing step involves three methods. The first method is noise removal using curvelet transform, next is artifact removal and last is skull removal using mathematical morphology. Segmentation is done using spatial FCM.

In [13], *Beham and Gurulakshmi* proposed a method consisting of three steps: The first step is image enhancement in which outer elliptical shaped object is eliminated. The second step is morphological processing, conducted for extracting the needed region. The final step is the segmentation using K-means clustering algorithm. This unsupervised method is efficient and less prone to error and can be carried out with lesser amount of data giving accurate output compared to supervised methods.

To overcome the deficiencies of existing techniques, we propose an improved technique which is efficient in denoising of images corrupted by Gaussian noise. Gaussian noise can be effectively removed by using the wavelet techniques because of the ability of the wavelet to capture the energy of the signal in few energy transform values [15]. Moreover, threshold selection is done using automated means which gets an optimized value for global thresholding.

III. PROPOSED SYSTEM

In this paper, we propose a new hybrid method using DWT, morphological operators, K-means and Otsu's thresholding technique for detecting and segmenting the tumor in the brain. DWT is used for image denoising. Morphological operators (erosion and dilation) are used for skull removal from the brain images. K-means clustering and thresholding approaches are used for image segmentation. This segmentation is finally used to detect the brain tumor. The flow graph shown in Figure 1 depicts the step by step procedure to be followed for detecting the tumor.

A. Image Acquisition

Images are acquired using non-invasive Magnetic resonance imaging (MRI) scan. The MRI scanner has a sliding table, which goes inside the circular apparatus during acquisition. A sample brain image using MRI scan is shown

in Figure 2 a) and then converted into grayscale as shown in Figure 2 b).

B. Image Denoising

In the proposed method, noise removal is done using DWT filtering. The wavelets are the functions that deal with both the frequency and the temporal components. Denoising of the images using wavelet technique is very effective, when images are degraded by Gaussian noise. This is because of their ability to capture the signal energy in few energy transform values [15]. The enhanced image after removing noise using DWT filtering is shown in Figure 2 c).

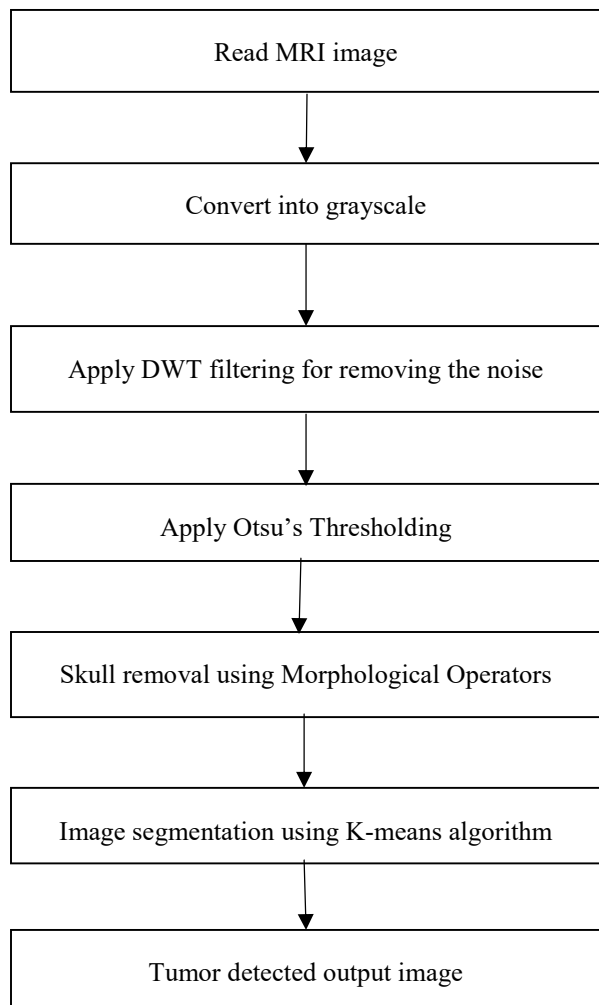


Figure 1. Proposed methodology for tumor detection.

C. Otsu's Thresholding

Otsu's thresholding is applied to the enhanced image after denoising using DWT filtering technique. The purpose of Otsu's thresholding method is to get an optimized value for global thresholding. In Otsu's thresholding, it is pre-assumed that image has 2 classes of pixels or a bimodal

histogram. The pixels in image are divided into two categories- foreground and background. The segmented image after applying Otsu's thresholding is shown in Figure 2 d).

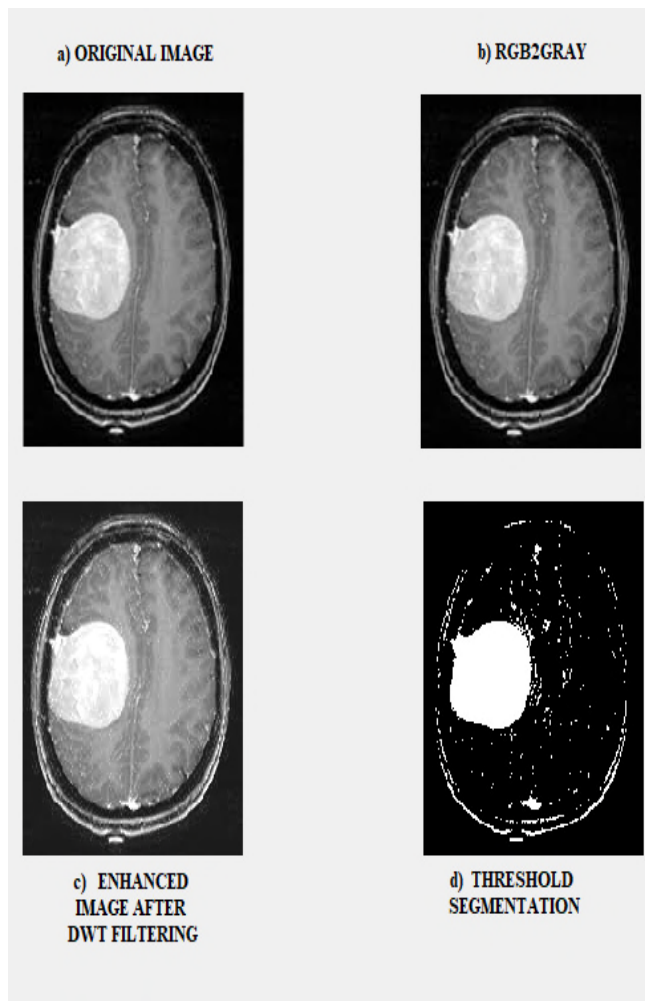


Figure 2. a) Input brain MRI image; b) Grayscale image; c) Enhanced image after denoising using DWT filtering; d) Image after applying Otsu's thresholding.

D. Skull Removal

The segmented image after Otsu's thresholding is taken as input to this stage. The skull removal means elimination of brain's non-cerebral tissues. There is a need to remove brain's skull portion as the skull portion is bright and its intensity is almost same as that of tumor and thus it can influence the segmentation of tumor.

In the proposed method, two basic morphological operators, erosion and dilation are used for removing the skull portions. Dilation fills the holes and equalizes the contour lines. Erosion, on the other hand, eliminates the small objects and detaches the object joined by small bridge. These morphological operators are based on a structuring element, that serves as a small window and scrutinize the

image. The choice of an appropriate structuring element is a must for proper removal of the skull portion [5]. The result of skull removal is shown in Figure 3.

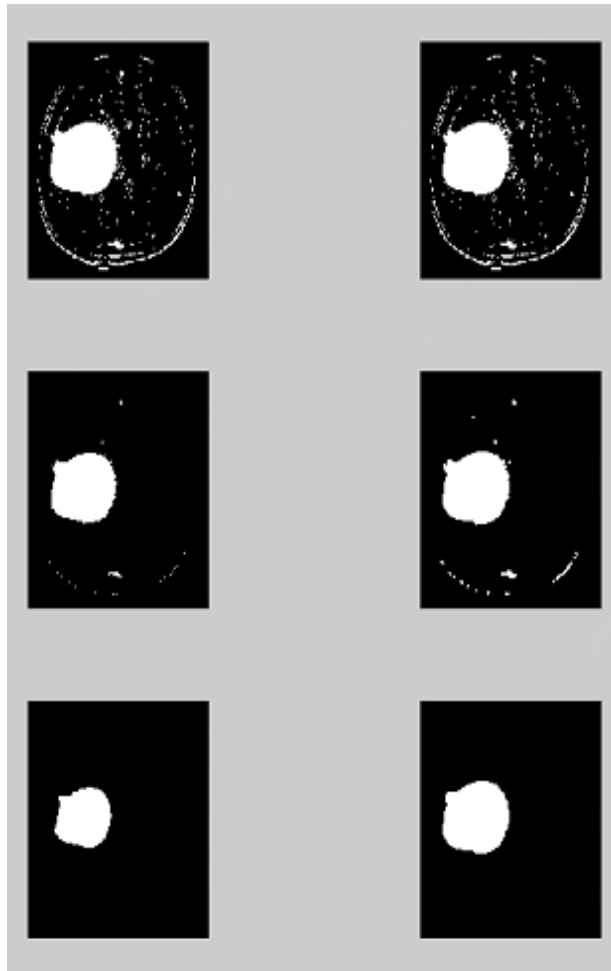


Figure 3. Skull removal after applying erosion (Left) and then dilation (Right) with structuring element ‘disk’ of radius 0,1,6 respectively from top to bottom.

E. Image Segmentation

Segmentation is the next important step to be carried out after image denoising and skull removal so as to precisely detect the tumor. Image Segmentation is the process of taking out the region of interest from an image by automated or semi-automated means [9]. There are various image segmentation methods such as watershed segmentation, thresholding, region growing, clustering, classification methods and so on [6].

In the proposed method, the image segmentation is performed using K-means clustering, an unsupervised method which is efficient and less prone to error and can be carried out with minimal data.

K-means [6] is an unsupervised method that divides the image into K- clusters on the basis of mean of each cluster. Initially, data is partitioned into K- clusters and thereafter

mean of each cluster is computed. Each point is then added to the cluster having the minimum distance to the clusters mean on the basis of Euclidean distance. The final detected tumor after K-means segmentation is shown in Figure 4.

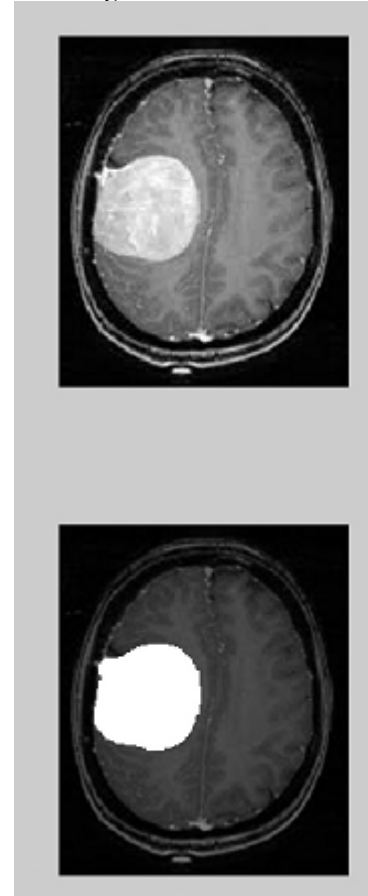


Figure 4: Final image of detected tumor using K- means segmentation.

IV. PERFORMANCE ANALYSIS

The proposed method is implemented on MATLAB (2010a) on a system having configuration Intel core 2 with processing speed 2.54 GHz, 2 GB RAM. There are various performance parameters for analyzing the images. The Peak Signal to Noise ratio (PSNR) [16] is one of the most important factor for analyzing the image. PSNR is the ratio of original image to noiseless image. For denoising methods, PSNR average value ranges between 20-50 dB. The formula to calculate the value of PSNR is given in (1) where MSE is the Mean Square Error.

$$PSNR = 10 \cdot \log_{10} \left[\frac{(MAX)^2}{MSE} \right] \quad (1)$$

The PSNR is used as a measure to reconstruct the image quality. The higher the PSNR value, the higher the image quality.

Mean Square Error (MSE) is another important measure for analyzing the image. MSE [16] is a risk function that corresponds to the expected value of squared error. The MSE is defined as:

$$MSE = 10 \cdot \log_{10} (\text{signal/noise}) \quad (2)$$

The smaller the value of MSE, the higher the image quality.

One more performance evaluation parameter is Bit Error Rate (BER) [17] defined as:

$$BER = 1/PSNR \tag{3}$$

The smaller the value of BER, the higher the image quality.

The values of MSE, PSNR, BER obtained by the proposed method, when implemented on MATLAB are shown in Figure 5.

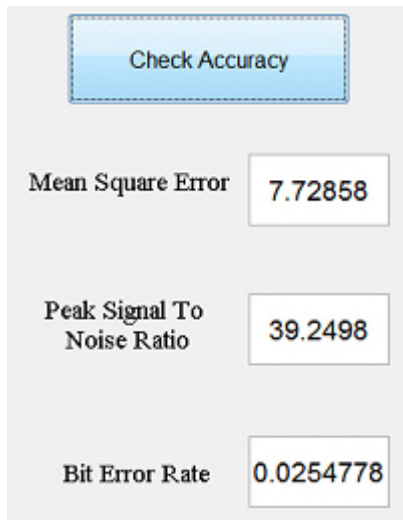


Figure 5: Result of MSE, PSNR, BER

The values of various performance parameters such as MSE, PSNR and BER obtained by the proposed technique are compared with the existing techniques in Table 1.

TABLE I. RESULT OF SEGMENTATION

Segmentation Techniques	MSE	PSNR	BER
Watershed Segmentation	2.0244	5.0677	0.19732
Region Growing Segmentation	9.5276	38.3749	0.02605
K-means and Otsu's Thresholding	7.7285	39.2498	0.02547

It can be observed from the Table 1 that the proposed method shows better results than the other existing methods. Here, the value of PSNR is more and the value of MSE and BER is less for the proposed method as compared to watershed and region growing segmentation.

V. CONCLUSION

Finding the accurate border of the area, comprising an identified brain tumor is a difficult task and needs to be addressed as it is applicable to many medical modalities

and tumor types. In this paper, we proposed a new hybrid method using DWT, morphological operators, K-means and Otsu's thresholding technique for detecting and segmenting the tumor in the brain. The proposed method efficiently detects the tumor from the brain MRI images. The result of the proposed method is compared with the existing methods and it was found that the values of MSE and BER are less and value of PSNR is high as compared to the existing watershed and the region growing segmentation. Lower values of MSE and BER and high value of PSNR result in better image quality.

In the future work of this study, we will attempt to modify the proposed technique so as to classify the type of tumor as benign, malignant, or pre-malignant.

REFERENCES

- [1] T. Lewis and S. Writer. Human Brain: Facts, Functions & Anatomy [Online]. Available: <http://www.livescience.com/29365-human-brain.html>, [Retrieved: August, 2018].
- [2] Anatomy of the Brain [Online]. Available: <http://www.mayfieldclinic.com/PDF/PE-AnatBrain.Pdf>, [Retrieved: August, 2018].
- [3] A. Mandal. (2014, Apr 02). What is a Brain Tumor? [Online]. Available: <http://www.news-medical.net/health/What-is-a-Brain-Tumor.aspx>, [Retrieved: August, 2018].
- [4] F. C. Harris, M. C. Gadiya, M. C. Motwani, and R. C. Motwani, "Survey of Image Denoising Techniques", Proc. GSPX, pp. 27-30, 2004.
- [5] L. Ramya and N.Sasirekha, "A Robust Segmentation Algorithm using Morphological Operators for Detection of Tumor in MRI," 2015 IEEE International Conference on Innovations in Information Embedded and Communication Systems ICIIECS 2015, pp. 1-4, 2015.
- [6] A. Norouzi et al. "Medical Image Segmentation Methods, Algorithms, and Applications," IETE Technical Review June 2014, vol. 31, no. 3, pp. 199-213, 2014.
- [7] M. B. Ayed, A. Kharrat, and M. B. Halima, "MRI Brain Tumor Classification using Support Vector Machines and Meta-Heuristic Method," International Conference on Intelligent Systems Design and Applications ISDA 2015, pp. 446-451, 2016.
- [8] S. E. El-Khamy, R. A. Sadek, and M. A. El-Khoreby, "An Efficient Brain Mass Detection with Adaptive Clustered based Fuzzy C-Mean and Thresholding," 2015 IEEE International Conference on Signal and Image Processing Applications ICSIPA 2015, pp. 429-433, 2015.
- [9] Image Segmentation [Online]. Available: <https://in.mathworks.com/discovery/image-segmentation.html>, [Retrieved: September, 2018].
- [10] N. N. Gopal and M. Karnan, "Diagnose Brain Tumor through MRI using Image Processing Clustering Algorithms such as Fuzzy C Means along with Intelligent Optimization Techniques," 2010 IEEE International Conference on Computational Intelligence and Computing Research ICCIC 2010, pp. 694-697, 2010.
- [11] R. G. Selkar and M. N. Thakare, "Brain Tumor Detection and Segmentation By Using Thresholding and Watershed Algorithm," International Journal of Advanced Information and Communication Technology IJAICT 2014, vol. 1, no. 3, pp. 321-324, 2014.
- [12] A. Lakshmi, T. Arivoli, and R. Vinupriyadharshini, "Noise and Skull removal of Brain Magnetic Resonance Image using Curvelet transform and Mathematical Morphology,"

- International Conference on Electronics and Communication Systems ICECS 2014*, pp. 1–4, 2014.
- [13] M. P. Beham and A. B. Gurulakshmi, “Morphological Image Processing Approach On The Detection Of Tumor and Cancer Cells,” *International Conference on Devices, Circuits and Systems (ICDCS)*, 2012, pp. 350–354, 2012.
- [14] R. C. Gonzalez and R. E. Woods, "Image Restoration," in *Digital Image Processing*, 2nd ed. New Jersey: Prentice-Hall, 2001, ch. 5, pp. 220-272.
- [15] M. M. Sathik, S. A. Perumal, and S. K. Mohideen, “Image De-noising using Discrete Wavelet Transform,” *International Journal of Computer Science & Network Security (IJCSNS)*, 2008, vol. 8, no. 1, pp. 213-216, January 2008.
- [16] P. Kaushik and Y. Sharma, “Comparison of Different Image Enhancement Techniques Based upon PSNR & MSE,” *International Journal of Applied Engineering and Research*, 2012, vol. 7, no. 11, 2012. ISSN 0973-4562.
- [17] G. Singh, S. Arora and V. K. Banga, “Comparison of F-measure, BER and PSNR of Tumor Detection using Hybridization of Fuzzy and Region Growing,” *International Journal of Computer Applications 2015*, vol.124, no. 3, pp. 32-38, August 2015.

A Phenomenological Model of Energy Relaxation in Disordered Insulators Irradiated by Ultrafast Proton Pulses

Lorenzo Stella*, Jonathan Smyth*, Brendan Dromey**

Atomistic Simulation Centre*, Centre for Plasma Physics**
School of Mathematics and Physics
Queen's University Belfast
Northern Ireland

Emails: l.stella@qub.ac.uk, jsmyth78@qub.ac.uk, b.dromey@qub.ac.uk

Abstract—The picosecond relaxation of an electronically excited insulator is described by means of an extension of the two-temperature model. In this phenomenological description, charge neutrality is enforced, but the electron and hole chemical potentials are not forced to be equal. Different experimental regimes can be characterized by comparing the electron-lattice and electron-hole relaxation rates. The dependency of the long-time relaxation on both the electronic gap and the sample density is discussed. The extend two-temperature model correctly describes the unexpectedly long transient opacity displayed by a borosilicate glass irradiated by ultrafast proton pulses.

Keywords—Proton irradiation; Insulators; Electron-hole plasma; Two-temperature model.

I. INTRODUCTION

By means of the target normal sheath acceleration mechanism, ultrafast (3 ± 0.8 ps) proton pulses with a very sharp energy (15 ± 1.5 MeV) can be generated at local-scale laser facilities, like the TARANIS multi-terawatt laser at Queen's University Belfast [1]. This novel experimental capabilities are ideally suited to investigate the relaxation of the electron-hole plasma generated upon proton irradiation of solids and liquids. For instance, the transient opacity of transparent insulators [2][3] and water [4] over a few hundreds of ps after the proton passage can be monitored using optical streaking. These early experiments have revealed an unexpectedly long (>100 ps) transient opacity in the near infrared (1054 nm probe). This unexpected behavior has been linked to the persistence of a 'cold' electron-hole plasma which causes the extinction of the probe.

In this paper, we introduce a simple extension of the Two-Temperature Model (TTM) [5] which describes the experimental results using two phenomenological time-scales. The first time-scale is related to the well-known electron-lattice (or electron-phonon) relaxation [6], while the second time-scale is related to the relaxation of the electrons and holes to a common 'chemical' equilibrium. In particular, we find that the transient opacity of an irradiated borosilicate (BK7) glass is well described by a short electron-phonon time-scale (<10 ps) — in agreement with previous estimates — and a longer 'chemical' relaxation time-scale of 110 ps. A microscopic

justification of the longer 'chemical' relaxation of the electron-hole plasma using an excitonic relaxation model [7][8] is currently attempted.

This paper is organized as follows: Section II describes the phenomenological kinetic equations used to model the experiments; Section III contains the main results of the paper; Finally, Section IV provides a brief discussion of the underlying microscopic mechanisms and a proposal for the validation of the model.

II. KINETIC MODEL

In order to model the electron-hole plasma generated upon proton irradiation, we made the following assumptions: i) The plasma is classical and Boltzmann statistics applies; ii) The plasma is well described by a gas of non-interacting particles (ideal gas); iii) The plasma is homogeneous, *i.e.*, the electron and hole concentrations do not depend on the position, \mathbf{r} ; iv) The electrons and holes have equilibrated separately, although a global equilibrium has not reached yet.

The first assumption is not crucial and will be relaxed (see Section III). The Boltzmann statistics is used here to keep the presentation simple and uncluttered. The second assumption is strictly justified at low concentration, but no attempt to include the many-body interaction is described in this paper. The third and fourth assumptions are valid after 10–100 fs, *i.e.*, the time it takes to the electrons and holes to diffuse about the proton track and equilibrate through fast collisional processes. These final assumptions can be independently validated by solving a set of coupled charge and energy transport equations [7] based on a convenient hydrodynamic approximation [9].

To model the long (>100 ps) relaxation dynamics probed by the experiments of Dromey *et al.* [2][3][4], the full solution of the coupled charge and energy transport equations, *e.g.*, using finite element models, still requires a considerable numerical effort. Those are equations for the electrostatic potential, $\phi(\mathbf{r}, t)$, the electron and hole concentrations, $n(\mathbf{r}, t)$ and $p(\mathbf{r}, t)$, the electron and hole temperatures, $T_n(\mathbf{r}, t)$ and $T_p(\mathbf{r}, t)$, and the lattice temperature, $T_l(\mathbf{r}, t)$. In view of our assumption iii), we can immediately set $\phi = 0$ and neglect the dependence on \mathbf{r} . Assumptions iv) implies that we

can use the equilibrium expression for the electron and hole concentrations,

$$n(t) = \left(\frac{2}{\Lambda_e^3} \right) \exp \left(\frac{\mu_e}{k_B T_e} \right) \quad (1)$$

and

$$p(t) = \left(\frac{2}{\Lambda_p^3} \right) \exp \left(-\frac{E_g - \mu_p}{k_B T_p} \right), \quad (2)$$

where k_B is the Boltzmann constant, Λ_e and Λ_p are the thermal wavelengths of the electrons and holes [10], μ_e and μ_p are the chemical potentials of the electrons and holes, and E_g is the band gap. Energies are measured from the bottom of the conduction band.

Global charge neutrality requires that $n(t) = p(t)$. By further assuming that $T_e = T_p$, it can be shown that $\mu_e = \bar{\mu} + \xi/2$ and $\mu_h = -\bar{\mu} + \xi/2$, where $\bar{\mu} = -(E_g/2) + (3k_B T/4) \ln(m_h/m_e)$ is the average chemical potential, and we will refer to $\xi = \mu_e + \mu_p$ as the chemical bias. At ‘chemical’ equilibrium between particle at holes, we have that $\mu_p = -\mu_e$ or $\xi = 0$. We conclude the paragraph by rephrasing assumption iv) as: The electron and holes are in thermal equilibrium with $T_e = T_p$, but not yet in ‘chemical equilibrium ($\xi > 0$).

As the electron-hole plasma evolves towards its ‘chemical’ equilibrium, the chemical bias, ξ , will decrease to zero. Concurrently, the plasma will evolve towards its thermal equilibrium with the lattice, reached when $T_e = T_l$. In view of this simple kinetic picture, we can write down the following coupled phenomenological equations:

$$\begin{cases} \left(\frac{\partial u}{\partial T_e} \right)_n \dot{T}_e = - \left(gn + \frac{1}{\tau_b} \left(\frac{\partial u}{\partial T_e} \right)_n \right) (T_e - T_l), \\ \left(\frac{\partial u}{\partial \xi} \right)_n \dot{\xi} = -gn(T_e - T_l) - \frac{1}{\tau_b} \left(\frac{\partial u}{\partial \xi} \right)_n \xi, \end{cases} \quad (3)$$

where g , and τ_b are model parameters, u is the energy density of the electron-hole plasma, and $(\partial x/\partial y)_n$ stands for the derivative of x with respect to y taken at fixed electron concentration.

First of all, the equilibrium solution $T_e = T_l$ and $\xi = 0$ is a stationary solution of Eq. (3). Secondly, in the limit of $\tau_b \rightarrow \infty$, the equations reduce to $(\partial u/\partial T_e)_n T_e = -gn(T_e - T_l)$, i.e., a simple convective heat transfer equation between the electron-hole plasma and the lattice [5].

To clarify the $\tau_b \rightarrow \infty$ limit, we substitute Eq. (3) into the time-derivative of the electron concentration and obtain that

$$\dot{n} = -\frac{1}{\tau_b} \left[\left(\frac{\partial n}{\partial T} \right)_\xi (T_e - T_l) + \left(\frac{\partial n}{\partial \xi} \right)_T \xi \right] \quad (4)$$

Hence, the electron concentration gets fixed when $\tau_b \rightarrow \infty$. As a consequence, the second line of Eq. (3) becomes redundant in the limit of $\tau_b \rightarrow \infty$. Also note that the last line of Eq. (4) represents a pseudo-first order ‘chemical’ kinetic with ‘reaction’ rate $1/\tau_b$. This ‘chemical reaction’ involves the non-radiative recombination of the electrons and holes.

The parameter, g , is related to the electron-phonon relaxation. It is worth noting that at the end of the proton irradiation experiment described in Refs. [2][3][4], the sample’s macroscopic optical properties are completely recovered. As a consequence, a relatively small amount of energy is

initially absorbed by the electron-hole plasma and eventually transferred to the lattice.

The time-derivative of the energy density of the electron-hole plasma is given by

$$\begin{aligned} \dot{u} = & -gn(T_e - T_l) \\ & -\frac{1}{\tau_b} \left[\left(\frac{\partial u}{\partial T_e} \right)_\xi (T_e - T_l) + \left(\frac{\partial u}{\partial \xi} \right)_T \xi \right] \end{aligned} \quad (5)$$

where in the first step we have used Eq. (4). By equating the energy lost by the electron-hole plasma to the energy gained by the lattice, we find the following equation for T_l ,

$$\begin{aligned} 3\rho_l N_A k_B \dot{T}_l = & gn(T_e - T_l) \\ & + \frac{1}{\tau_b} \left[\left(\frac{\partial u}{\partial T_e} \right)_\xi (T_e - T_l) + \left(\frac{\partial u}{\partial \xi} \right)_{T_e} \xi \right], \end{aligned} \quad (6)$$

where ρ_l is the molar density of the lattice and N_A is the Avogadro number.

In the limit of $\tau_b \rightarrow \infty$, the combined Eq. (3) and Eq. (6) give the well-known homogeneous TTM defined by

$$\begin{cases} \left(\frac{\partial u}{\partial T_e} \right)_n \dot{T}_e = -g'(T_e - T_l), \\ 3\rho_l N_A k_B \dot{T}_l = g'(T_e - T_l), \end{cases} \quad (7)$$

where $g' = gn$. Note that Eq. (7) has been used for modeling energy relaxation in metals [5], in which the electron concentration, n , is indeed fixed. We can then conclude that Eq. (3) along with Eq. (6) provide a simple phenomenological extension of the homogeneous TTM to the case in which the electron concentration is not fixed.

We end the section by mentioning that Eq. (3) satisfies the Onsager’s reciprocal relations [10] and that all the equilibrium properties of our electron-hole plasma model can be obtained from grand potential density

$$\Omega(T_e, \xi) = - \left(\frac{4k_B T_e}{\Lambda_e^3} \right) \exp \left(\frac{\bar{\mu}}{k_B T_e} + \frac{\xi}{2k_B T_e} \right), \quad (8)$$

or its straightforward extension to the degenerate case. For instance, we have that (see Eq. (1))

$$n = p = -(\partial \Omega / \partial \xi)_{T_e} \quad (9)$$

III. RESULTS

In the experiments of Dromey *et al.* [2][3][4], the transient opacity of a transparent insulator is probed upon ultrafast proton irradiation. A 1053 nm infrared source is used as a probe. To interpret this kind of experiments, we assumed that the extinction is due to free carrier (electrons and holes) and we use a Drude model,

$$\epsilon(\omega) = \epsilon_\infty - \frac{\omega_p^2}{\omega(\omega + i\gamma)}, \quad (10)$$

of the dielectric permittivity of the electron-hole plasma. In Eq. (10), ϵ_∞ is the dielectric permittivity of the transparent insulator (host material), $\omega_p = \sqrt{e^2 n / \epsilon_0 \bar{m}}$ is the plasmon frequency, with $1/\bar{m} = (1/m_e) + (1/m_p)$ being the reduced electron-hole mass, and γ is a phenomenological relaxation rate. The density, n , appearing in the plasmon frequency is obtained from Eq. (1) upon integration of the coupled

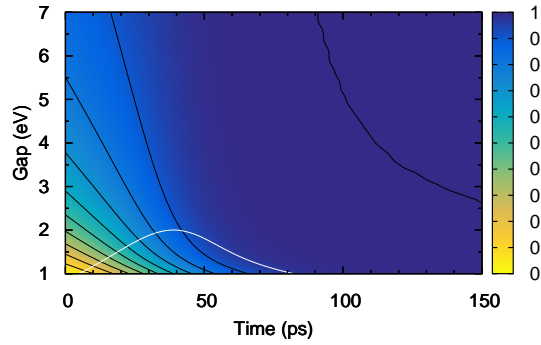


Figure 1. Map of the transmittance as function of the band gap and time, at fixed molar density. The the band gap of BK7 glass is approximately 3.5 eV, see text for the fixed model parameters. In the the region below the white line the electron-hole plasma is degenerate.

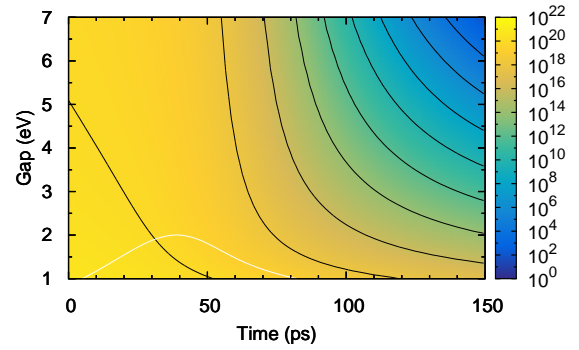


Figure 2. Map of the electron-hole pair density as function of the band gap and time, at fixed molar density. The the band gap of BK7 glass is approximately 3.5 eV, see text for the fixed model parameters. In the the region below the white line the electron-hole plasma is degenerate.

phenomenological equations, Eqs. (3) and (6). The results presented in this section are obtained using Fermi-Dirac statistics, although Boltzmann statistics gives a good approximation for most of the parameter values.

Following the experiments [2], we assume an average track density, of 50 tracks per μm^2 . Defining an effective track radius, R , the track polarizability is found as

$$\alpha(\omega) = 2\epsilon_0 \left(\frac{\epsilon(\omega) - \epsilon_\infty}{\epsilon(\omega) + \epsilon_\infty} \right) \pi R^2 \quad (11)$$

Finally, the extinction cross-section (dimensionally, it is a length, not an area) of the a track is

$$\sigma_{ext}(\omega) = \frac{k}{\epsilon_0} \text{Im} \{ \alpha(\omega) \} + \frac{k^4 |\alpha(\omega)|^2}{6\pi\epsilon_0^2}, \quad (12)$$

where the first term accounts for the absorption and the second one for the scattering [11]. The wave number is $k = \omega\sqrt{\epsilon_\infty}/c$, where c is the speed of light.

To fit the observed transient opacity of BK7 glass, we set the band gap, $E_g = 3.5$ eV, the sample molar density $\rho_l = 0.04$ mol/cm³, and the refraction index, $\sqrt{\epsilon_\infty} = 1.5$. As an initial guess, we also set $m_p = m_e = 0.5$ mass of the electron. The stopping power of 15 MeV protons close to the Bragg peak is approximately $S_e = 12$ eV/Å [12]. The initial electron concentration is then set to $n_0 = (S_e/\pi R^2)/3E_g$ and the initial temperature to $T_0 = 2E_g/3k_B$ [7]. The initial condition fro the chemical bias, ξ_0 , is found by solving $n_0 = n(T_0, \xi_0)$ (see Eq. (1)). Finally, we set the effective track radius as $R = 5$ nm. Given these physical parameters, a good fit of the experimental data is compatible with the following values of the free parameters: $\gamma = 17$ meV, $g = 2.5 \cdot 10^{-12}$ W/K, and $\tau_b = 110$ ps.

To get some insight into the qualitative behavior our model, we perform a ‘sensitivity analysis’ varying two physical parameters, E_g and ρ_l , while keeping fixed all the remaining parameters, including γ , g , and τ_b .

Figure 1 shows a map of the time-dependent transmittance as a function of the band gap. As a general trend, the transient opacity gets more pronounced and longer lived as the band gap decreases. For instance, amorphous silica, having a band gap

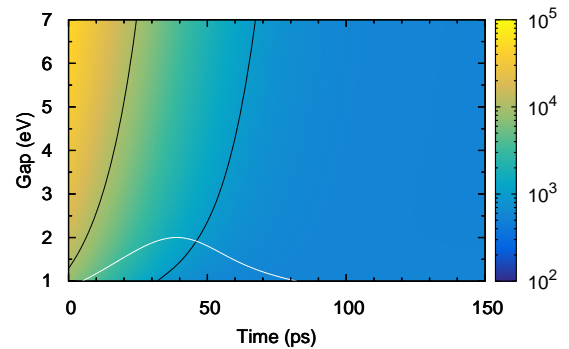


Figure 3. Map of the electronic temperature as function of the band gap and time, at fixed molar density. The the band gap of BK7 glass is approximately 3.5 eV, see text for the fixed model parameters. In the the region below the white line the electron-hole plasma is degenerate.

of about 9 eV and a molar density similar to that of the BK7 glass, is predicted to display a negligible transient opacity in an analogous proton irradiation experiment.

The trend with transmittance is well matched by the trend with electron-holes pair density, as shown in Figure 2. The match directly follows from our hypothesis that the transient opacity is due a sizable free carrier (electrons and holes) extinction upon proton irradiation.

The longer lived transient opacity is anti-correlated with the peak electronic temperature, as shown in Figure 3. This anti-correlation is a consequence of the competition between two relaxation mechanisms: 1) Thermal relaxation between the electron-hole plasma and the lattice; 2) ‘Chemical’ relaxation between electrons and holes. According to our model, the thermal relaxation mechanism is slower than the ‘chemical’ one for wide gap insulators, while the opposite is true for smaller gap insulators. In particular, the long lived transient opacity can be ascribed to persistent ‘cold’ (*i.e.*, in thermal equilibrium with the lattice) electron-hole plasma.

Finally, Figure 4 shows a map of the time-dependent transmittance as a function of the molar density. In this case, the transient opacity gets more pronounced and longer lived

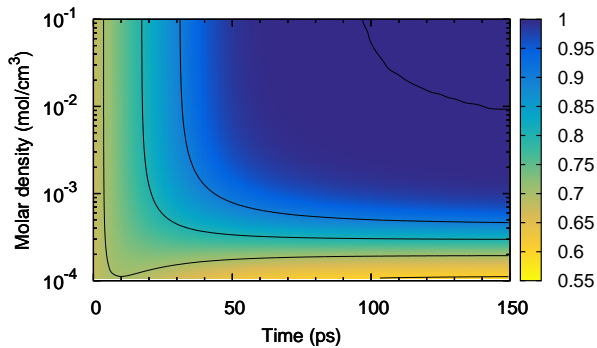


Figure 4. Map of the transmittance as function of the molar density and time, at fixed band gap. The molar density of BK7 glass is approximately 0.04 mol/cm^3 , see text for the fixed model parameters.

as the molar density decreases. Given the linear dependency of the heat capacity of the lattice on the molar density (see Eq. (6)), the thermal equilibrium between the electron-plasma and the lattice is quickly reached at a larger electronic temperature, T_e . As a consequence, the electron concentration is also larger and the electron-hole plasma extinction enhanced. Heat diffusion across the lattice will eventually cause the hot proton track to equilibrate to the temperature of the surrounding host material, namely room temperature. The competition between the thermal relaxation mechanism and the thermal diffusion is not considered in this paper.

IV. DISCUSSION AND CONCLUSIONS

The phenomenological equations Eq. (3) and Eq. (6) provide a simple extension of the TTM to the case in which the electron concentration is not fixed. They can be readily generalized to include inhomogeneous electron and lattice temperatures, as in the inelastic thermal spike model [6]. Our proposal is complementary to the work of Daraszewicz and Duffy [13], who have extended the TTM by including an equation of motion for the electron concentration, n . In our proposal, n is a function of the electronic temperature, T_e , and the chemical bias, ξ . In particular, n is thermodynamically conjugated to ξ (see Eq. (9)). Using ξ is convenient because the ‘chemical’ equilibrium condition between electrons and holes, $\xi = 0$, is easily stated and enforced into the phenomenological equations.

From the fit of the experimental results, we obtain reasonable values of the free parameters γ and g . For a metal like iron, $n \approx 1.7 \cdot 10^{23} \text{ cm}^{-3}$, which gives $g' = gn \approx 4.3 \cdot 10^{11} \text{ W/cm}^3 \cdot \text{K}$, which compares favorably with the values found in literature [14]. On the other hand, the free parameter τ_b is inherent to our model and needs some microscopic justification. Starting from the early suggestion that an electron-hole plasma primarily decay into excitons [7], we assume that a ‘chemical’ equilibrium between the electron-hole plasma and the free excitons is rapidly reached. Hence, the rate-determining mechanism can be the slower (*i.e.*, activated) decay of the free excitons into self-trapped excitons [8]. The validation of this mechanism, along with other microscopic assumptions of the model, is currently attempted based on the full solution of the coupled charge and energy transport

equations.

ACKNOWLEDGMENTS

The authors would like to acknowledge financial support from EPSRC, grant EP/P016960/1, as well as useful conversations with A. Rivera, A.A. Correa, D. Duffy, and J. Kohanoff.

REFERENCES

- [1] T. Dzelzainis et al., “The taranis laser: A multi-terawatt system for laser-plasma investigations,” *Laser and Particle Beams*, vol. 28, 2010, pp. 451–461.
- [2] B. Dromey et al., “Ultrafast opacity in borosilicate glass induced by picosecond bursts of laser-driven ions,” 2014, unpublished. [Online]. Available: <https://arxiv.org/abs/1412.1327>
- [3] B. Dromey et al., “Picosecond metrology of laser-driven proton bursts,” *Nat. Commun.*, vol. 7, 2016, p. 10642.
- [4] M. Taylor et al., “Probing ultrafast proton induced dynamics in transparent dielectrics,” *Plasma Phys. Control. Fusion*, vol. 60, 2018, p. 054004.
- [5] M. Kaganov, E. Lifshitz, and L. Tanatarov, “Relaxation between electrons and the crystalline lattice,” *Sov. Phys. JETP*, vol. 4, 1957, pp. 173–178.
- [6] M. Toulemonde, W. Assmann, C. Dufour, A. Meftah, Studer, and C. Trautmann, “Experimental phenomena and thermal spike model description of ion tracks in amorphisable inorganic insulators,” *Mat. Fys. Medd.*, vol. 52, 2006, pp. 263–292.
- [7] S. Klaumünzer, “Thermal-spike models for ion track physics: A critical examination,” *Mat. Fys. Medd.*, vol. 52, 2006, pp. 293–328.
- [8] A. Rivera, J. Olivares, G. Garcia, and F. Agulló-López, “Swift heavy ion damage to sodium chloride: synergy between excitation and thermal spikes,” *J. Phys. Condens. Matter*, vol. 24, 2012, p. 085401.
- [9] T. Grasser, T.-W. Tang, H. Kosina, and S. Selberherr, “A review of hydrodynamic and energy-transport models for semiconductor device simulation,” *Proceedings of the IEEE*, vol. 91, 2003, pp. 251–274.
- [10] L. Landau and E. Lifshits, *Statistical Physics*, 3rd ed., ser. Course of theoretical physics. Pergamon Press, London, 1980, vol. 5.
- [11] C. Bohren and D. Huffman, *Absorption and Scattering of Light by Small Particles*, 1st ed. Wiley, New York, 1998.
- [12] M. Berger, J. Coursey, M. Zucker, and J. Chang. *Estar, pstar, and astar: Computer programs for calculating stopping-power and range tables for electrons, protons, and helium ions*. Online. NIST. (version 2.0.1). [Online]. Available: <http://physics.nist.gov/Star> [retrieved: July, 2017]
- [13] S. Daraszewicz and D. Duffy, “Extending the inelastic thermal spike model for semiconductors and insulators,” *Nucl. Instr. Meth. B*, vol. 269, 2011, pp. 1646–1649.
- [14] A. Dunlop, D. Lesueur, P. Legrand, H. Dammak, and J. Dural, “Effects induced by high electronic excitations in pure metals: A detailed study in iron,” *Nucl. Instr. Meth. B*, vol. 90, 1994, pp. 330–338.

Ultrafast Photoionization and Energy Absorption in Bulk Silicon and Germanium

Tzveta Apostolova^{1,2}

¹Institute for Nuclear Research and Nuclear Energy,
Bulgarian Academy of Sciences

²Institute for Advanced Physical Studies,
New Bulgarian University
Sofia, Bulgaria
e-mail: tzveta@innrne.bas.bg

Boyan Obreshkov

Institute for Nuclear Research and Nuclear Energy,
Bulgarian Academy of Sciences

Sofia, Bulgaria
e-mail: obreshko@innrne.bas.bg

Abstract— Intense femtosecond laser pulses are routinely used to stimulate ultrafast transformations in the properties of the dielectric materials. Understanding the connection of the microscopic response with the macroscopic properties of the photoexcited material, requires application of space and time resolved experimental techniques and development of predictive theoretical tools to rationalize experimental data. In the field of modeling ultrashort laser-matter interactions, progress has been achieved in understanding photoionization and atomic scale properties of ultrafast electronic currents within the Time Dependent Density Functional Theory. However, first-principles approaches for description of micro- and macroscopic material responses are usually limited to ultrashort time scales of order 10fs, since the calculation is time consuming and requires large computational resources. We overcome this limitation by applying the empirical pseudopotential method for describing the electronic properties of dielectric materials. The deposited energy, photoelectron densities, ultrafast currents and optical breakdown thresholds in bulk silicon and germanium, irradiated by intense 30 fs pulsed laser with near-infrared and mid-infrared wavelengths (800nm-5 μ m) and intensities 1GW/cm²-1TW/cm² are obtained by solving the time-dependent Schrodinger equation in single active electron approximation.

Keywords- group IV semiconductors; femtosecond laser irradiation; nonthermal melting; nonlinear optical properties; multiphoton and tunnel ionization.

I. INTRODUCTION

Femtosecond laser irradiation is suitable for studying fundamental processes in solids, such as ultrafast chemical reactions and phase transitions. Photoionization and photoexcitation of electrons in solids is the predominant mechanism of laser-pulse energy deposition, which subsequently may induce ultrafast transformation of the material. Depending on the laser parameters (wavelength, polarization, pulse energy and pulse duration), transformations of solid-state properties may be reversible or irreversible. Intense laser field may strongly distort the electronic structure by transiently converting insulators and dielectrics into metallic state on a sub femtosecond scale [1]. This distortion results in optical-field-induced transient and reversible currents below the bulk damage threshold [2]. For

sufficiently strong laser fields close to the bulk damage threshold, irreversible transformation occurs resulting in non-thermal melting [3], sublimation and ablation on a longer time scale. When intense ultrashort laser pulse is used for material modification, the different stages during the phase transformation can be studied using time-resolved techniques. Study of the nonthermal melting of germanium using ultrafast x-ray diffraction techniques was reported and it was assumed that this ultrafast process takes place when ~10% of the valence-band electrons are excited to the conduction band [4]. The ultrafast phase transitions and the dynamics of melting, ablation and re-solidification of germanium surfaces was studied [5] using space- and time-resolved measurements of the surface reflectivity.

At the same time, femtosecond laser interaction of semiconductors has found important practical applications, e.g. the graphitization of diamond bulk and creation of color centers could be used in quantum information processing and the manipulation of qubits [6]. Laser-induced graphitization in bulk diamond is used in the design of particle detectors [7]. Dielectric surfaces can be promptly converted into plasmonic state by ultrafast laser irradiation, supporting propagation of surface plasmon-polaritons. For instance, the plasmonic properties of silicon and germanium can be used for metamaterial applications at near-infrared and mid-infrared wavelengths [8][9].

Ultrafast phase transformation of semiconductors under intense femtosecond irradiation starts with photoionization and deposition of laser energy onto the electrons. In this paper, we study the nonlinear response of silicon and germanium irradiated by intense near-IR and mid-IR laser pulses with time duration of 30 femtoseconds. For this purpose, we have developed numerical methods for integration of the time-dependent Schrodinger equation in single active electron approximation [10]-[13].

More specifically, we estimate optical breakdown thresholds of silicon and germanium from the deposited laser energy inside the bulk. We find two regimes of absorption: at lower intensities, the absorbed energy depends sensitively on the laser wavelength due to multiphoton transitions, and a crossover occurs at higher intensity, when absorption becomes wavelength-independent. The merging point in laser intensity is material specific. In the multi-photon absorption regime, the dependence of the absorbed energy on the driving laser intensity is determined and scaling laws are obtained. For mid-IR wavelengths, we find that a smaller

number of photons is required to cross the direct bandgap as compared to the minimum number of photons allowed by energy conservation. For near-IR wavelengths, the scaling law exhibits a perturbative trend for both materials. At high intensity, the absorbed energy is wavelength independent and scales linearly with the laser intensity. This paper is organized as follows: Section II presents material and laser specific parameters which are inputs for the numerical solution of Time Dependent Schrodinger Equation. The numerical results for the photoelectron density and absorbed energy are discussed in section II A. The time evolution of the laser energy transfer to electrons, their number density and the ultrafast macroscopic currents are discussed in Section II B. Our main conclusions are included in Section III.

II. NUMERICAL RESULTS AND DISCUSSION

A. Photoelectron density and absorbed energy

The photon energies corresponding to the four wavelengths used in the calculations are: 1.55 eV (800 nm), 1.24 eV (1 μm) for near-IR irradiation, and 0.41 eV (3 μm), 0.248 eV (5 μm) for the mid-IR laser. The band-structures of Si and Ge were obtained numerically using the empirical pseudo-potential method [14]. The corresponding bulk lattice constants and selected transition energies between valence and conduction band states in the Brillouin zone are shown in Table 1. The calculated threshold for indirect electronic excitations in Ge is 0.9 eV and it is 0.8 eV for Si. In long wavelength approximation, the laser pulse ionizes electrons through the direct band gaps, the threshold for direct transitions in Ge is 1.2 eV and the corresponding threshold in Si is 3.4 eV.

TABLE I. BULK LATTICE CONSTANTS AND SELECTED BANDGAP ENERGIES IN GERMANIUM AND SILICON

	Lattice constant [Å]	$\Gamma_{25'}-\Gamma_{2'}$ [eV]	$\Gamma_{25'}-\Gamma_{15}$ [eV]	$\Gamma_{25'}-L_1$ [eV]	$\Gamma_{25'}-X(\Delta_1)$ [eV]
Ge	5.66	1.2	3.4	0.9	1.0
Si	5.43	3.9	3.4	1.8	0.8

In Fig. 1 and Fig. 2 we show the number of conduction electrons N_e produced by photoionization of silicon and germanium as a function of laser intensity after the irradiation with near-IR pulse of wavelength 800 nm. The number of photoelectrons in silicon increases monotonously with the increase of the laser intensity and follows a perturbative trend $N_e \sim I^2$ due to two-photon transition across the minimal direct bandgap. At the highest intensity shown (1.0 TW/cm^2), $N_e = 0.08$. For the same laser wavelength, similar results are found using the Time Dependent Density Functional Theory and the number of photoelectrons per atom at 1.0 TW/cm^2 obtained by the authors is $N_e = 0.06$ [15].

The intensity dependence of the number of photoelectrons in germanium, shown in Fig. 2, exhibits the same trend $N_e \sim I^2$ due to above threshold ionization via two photon transition from the light hole to the conduction band

involving Bloch crystal momentum displaced from the Brillouin zone center. When the laser peak intensity reaches 0.1 TW/cm^2 we find a change of slope in the photoionization yield following linear trend with $N_e \sim I$. At the highest intensity shown (1.0 TW/cm^2) the number of conduction electrons per atom is $N_e = 0.07$.

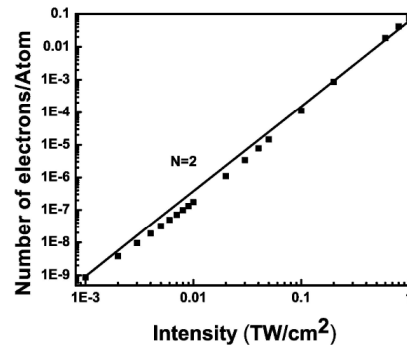


Figure 1. Intensity dependence of the number of conduction electrons per atom in bulk Si after the irradiation with 30fs near infrared pulse with wavelength 800 nm. The laser is linearly polarized along the [111] direction.

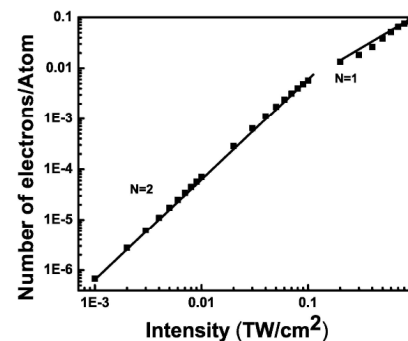


Figure 2. Intensity dependence of the number of conduction electrons per atom in bulk Ge after the irradiation with 30fs near infrared pulse with wavelength 800 nm. The laser is linearly polarized along the [111] direction.

Fig. 3 and Fig. 4 show the intensity dependence of the energy transferred to electrons in bulk Ge and Si after the irradiation with near-IR and mid-IR pulses. We distinguish two regimes of electronic excitation based on the scaling of the absorbed energy with the laser intensity. In the high-intensity regime the absorbed energy becomes independent of the laser wavelength above material-specific threshold intensity - 0.5 TW/cm^2 for Ge, and 1.0 TW/cm^2 for Si. The absorbed energy per Ge atom is 0.2 eV at threshold intensity, and is 0.28 eV per Si atom. Both absorbed energies at threshold are above the melting temperatures of the two materials - 0.104 eV (1211 Kelvin) for Ge and 0.145 eV (1687 Kelvin) for Si, respectively [16]. In this high intensity regime we find that the ultrafast energy deposition inside the bulk is sufficient to cause nonthermal melting. The low-intensity regime is wavelength dependent and is characterized by a superlinear scaling of the absorbed energy as a function of the intensity $\Delta E \sim I^N$. When $N = N_{\min}$, where N_{\min} is the minimum number of photons required to bridge

the direct band gap, perturbative multiphoton absorption is expected.

Fig. 3 shows the intensity dependence of the deposited laser energy in Ge. In the low-intensity regime, we obtain $N=2$ for irradiation with 800 nm wavelength, while resonant one-photon absorption is expected with $N_{\min}=1$. For the 1 μm wavelength, the same trend is observed for laser intensities below 5 GW/cm^2 . In the high intensity regime, the absorbed energy scales linearly with the laser intensity. For irradiation with mid-IR pulse having a 3 μm wavelength, we find $N=1$ for intensities up to 3 GW/cm^2 , which is less than the minimal number of photons required to cross the direct bandgap $N_{\min}=2$, however $N=N_{\min}=2$ in the range from 3 GW/cm^2 up to the threshold intensity for Ge. For 5 μm wavelength, in the range below 2 GW/cm^2 , $N=1$, for intensities 2 GW/cm^2 - 8 GW/cm^2 , $N=N_{\min}=4$, and $N=2$ for laser intensities above 15 GW/cm^2 .

Fig. 4 shows the intensity dependence of the deposited laser energy in silicon. In the low-intensity regime and in the near-IR region for the 800 nm wavelength, we find perturbative trend in the whole intensity range with $N_{\min}=N=2$, corresponding to two-photon absorption process, while for the 1 μm wavelength, three-photon transition occurs with $N=N_{\min}=3$ for all intensities considered. For irradiation with Si with mid-IR laser, we find that there is a threshold intensity 10 GW/cm^2 below which no laser energy is absorbed into the material. For the 3 μm wavelength, and laser intensity above this threshold, the absorbed energy exhibits the superlinear trend with $N=6$, which is less than the minimum number of photons required to cross the direct bandgap ($N_{\min}=8$). For 5 μm wavelength, a similar trend is observed: there is a step-like increase of the absorbed energy with $N=7$ and strong deviation from perturbative trend with $N_{\min}=13$. It is worth noting that for irradiation with 30 fs mid-IR laser pulses, the pulse length is a small multiple of an optical cycle. In this regime the tunnel ionization of electrons is expected to become dominant mechanism.

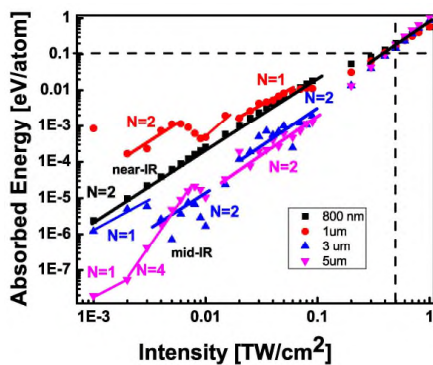


Figure 3. Intensity dependence of the energy absorbed per atom in bulk Ge irradiated by 30 fs laser pulse with laser wavelengths - (square) 800 nm, (circle) 1 μm , (triangle) 3 μm and (inverted triangle) 5 μm . The laser pulses are linearly polarized along the [111] direction. The horizontal dashed line indicates the energy corresponding to the melting temperature of the material and the vertical dashed line designates the position of the threshold intensity above which the deposited energy is wavelength independent.

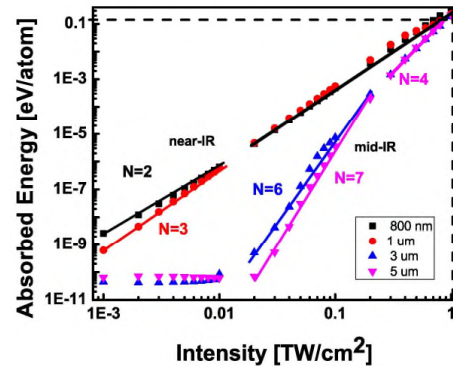


Figure 4. Intensity dependence of the energy absorbed per atom in bulk Si irradiated by 30 fs laser pulse with laser wavelengths - (square) 800 nm, (circle) 1 μm , (triangle) 3 μm and (inverted triangle) 5 μm . The laser pulses are linearly polarized along the [111] direction. The horizontal dashed line indicates the energy corresponding to the melting temperature of the material and the vertical dashed line specifies the position of the threshold intensity above which the deposited energy is wavelength independent.

B. Transient number density, absorbed energy and ultrafast macroscopic currents

The ultrafast laser energy deposition and the typical electron dynamics in the bulk of the two photoexcited materials is shown in Fig.5 - Fig.8 for two cases of different laser intensities, 0.05 TW/cm^2 and 0.6 TW/cm^2 . Fig. 5 (a) shows the transient electron densities in Ge for peak laser intensity 0.05 TW/cm^2 , corresponding to the four different wavelengths discussed in Sec. II A. The photoelectron density displays transient oscillations due to non-linear response of electrons, associated with the generation of intense second harmonic. The amplitude of these transient density oscillations increases substantially when the laser wavelength increases from near-IR to mid-IR region. Charge-carrier generation occurs on the rising edge of the pulse and competes with recombination of electron-hole pairs after the pulse peak to determine the final photoionization yield. A hot electron-hole plasma with number density of around 10^{20} cm^{-3} (near-IR wavelengths) and below 10^{19} cm^{-3} (mid-IR wavelengths) is established after the end of the pulse. Fig. 5 (b) shows the temporal evolution of the absorbed energy in bulk Ge after irradiation with peak laser intensity 0.05 TW/cm^2 . The absorbed energy displays oscillatory behavior dependent on the laser wavelength. For irradiation with near-IR laser, energy is efficiently transferred to the electronic system on the rising edge of the pulse. For irradiation with mid-IR wavelengths, large-amplitude transient fluctuations of the energy are exhibited during the pulse, but no significant amount of energy is transferred to electrons after the end of the

pulse.

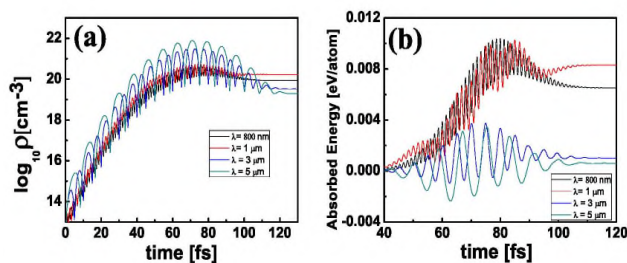


Figure 5. Transient electron density (a) and absorbed energy per atom (b) in bulk Ge irradiated by laser pulses of different wavelengths (indicated in the legend). The laser pulses are linearly polarized along the [111] direction and their peak intensity is 0.05 TW/cm².

For the higher intensity 0.6 TW/cm², shown in Fig. 6, the transient fluctuations of the absorbed energy are strongly suppressed during the irradiation with near-infrared pulse (cf. Fig. 6 (b)), however large amplitude of the oscillations is still prominent for mid-infrared wavelengths, particularly for the 5 μm wavelength. The deposited laser energy after the end of the pulse is wavelength independent. A similar trend is exhibited in the number density: regardless on the laser wavelength, an electron-hole plasma with number density of 10²¹ cm⁻³ is established after the pulse peak, cf. Fig. 6 (a).

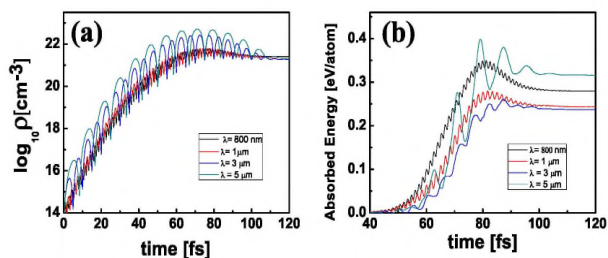


Figure 6. Transient electron density (a) and absorbed energy per atom (b) in bulk Ge irradiated by laser pulses of different wavelengths (indicated in the legend). The laser pulses are linearly polarized along the [111] direction and their peak intensity is 0.6 TW/cm².

Fig. 7 (a-b) shows the temporal evolution of the absorbed energy and photoelectron density in bulk Si for peak laser intensity 0.05 TW/cm², corresponding to the four different wavelengths discussed in Sec. IIA. Similar to the case of photoexcited Ge, laser induced oscillatory dynamics of electrons is exhibited. The amplitude of the transient energy fluctuations is large for all four wavelengths during the pulse. The absorbed energy after the end of the pulse is highly inefficient for both near infrared and mid-infrared wavelength regimes as seen in Fig. 7 (b). For near-IR wavelengths, the density of electron-hole pairs at the pulse peak is 10²⁰ cm⁻³, and this number density is reduced with two orders of magnitude to 10¹⁸ cm⁻³ after the end of the pulse as shown in Fig. 7 (a). For mid-IR laser, the

fluctuation in the number of conduction electrons is strongly enhanced during the irradiation: the density of electron-hole pairs at the pulse peak reaches 10²² cm⁻³. The virtual population of the conduction band disappears after the pulse peak and the number density of the generated real charge carriers is substantially reduced below 10¹⁵ cm⁻³.

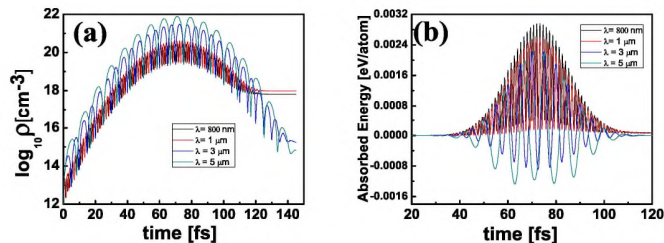


Figure 7. Transient electron density (a) and absorbed energy per atom (b) in bulk Si irradiated by laser pulses of different wavelengths (indicated in the legend). The laser pulses are linearly polarized along the [111] direction and their peak intensity is 0.05 TW/cm².

For the higher intensity 0.6 TW/cm², shown in Fig. 8 (a-b), the transient oscillations in energy are reduced for near infrared wavelengths and energy is efficiently absorbed after the end of the pulse as seen in Fig. 8 (b). The comparison between Fig. 6 (b) and Fig. 8 (b), shows that energy is much less efficiently absorbed in Si as compared to Ge for the same laser irradiation conditions. This is reasonable in view of the much larger direct bandgap in Si. Energy absorption is less efficient for 1 μm compared to 800 nm. For 5 μm, the transient fluctuations of the energy overshoot during the pulse with very high amplitude, indicating very efficient transient energy transfer to electrons. After the end of the pulse, energy absorption in bulk Si is 4 times more efficient for near-infrared wavelengths than for the mid-infrared ones. The density of the hot electron-hole plasma is around 10²⁰ cm⁻³ (for near-IR wavelengths) and is around 10¹⁹ cm⁻³ (for mid-IR wavelengths) as shown in Fig. 8 (a).

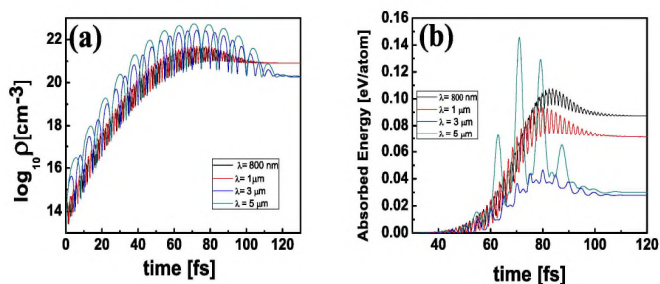


Figure 8. Transient electron density (a) and absorbed energy per atom (b) in bulk Si irradiated by laser pulses of different wavelengths (indicated in the legend). The laser pulses are linearly polarized along the [111] direction and their peak intensity is 0.6 TW/cm².

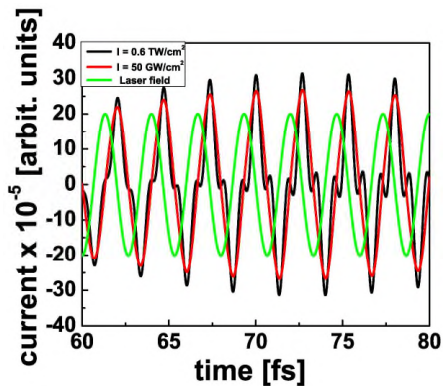


Figure 9. Induced electric currents in bulk Si for two intensities 0.05 TW/cm² (red) and 0.6 TW/cm² (black) and the applied laser field with wavelength 800 nm.

Fig. 9 shows the time evolution of the laser induced macroscopic currents inside the bulk Si during the irradiation with near-IR pulse of wavelength 800nm: two electric current waveforms, corresponding to the low and high laser intensity regimes - 50 GW/cm² and 0.6 TW/cm² are plotted, and the temporal profile of the driving laser field is shown. At the lower intensity of 50 GW/cm², the induced electric current lags behind the driving electric field by $\pi/2$, which indicates linear response of silicon. For that reason, energy transfer to electrons is unlikely, because negligible amount of work is done on the electron system by the driving laser field during each half-cycle. At the higher laser intensity - 0.6 TW/cm², the current still lags behind by nearly $\pi/2$ relative to the driving field, but the transient current develops a rapid subcycle structure due to nonlinear response of the electrons. As a consequence an efficient transfer of laser energy to the electrons occurs during each half cycle, the cumulative effect of these sub-cycle energy transfers eventually results in dielectric breakdown.

III. CONCLUSIONS AND FUTURE WORK

We have presented theoretical/numerical results of photo-excitation and energy absorption in Ge and Si, irradiated with intense, ultrashort laser pulses of 30 fs, using time-dependent Schrodinger equation in single active electron approximation. We obtained the wavelength and laser intensity dependence of the absorbed energy in the bulk of the materials. After the irradiation with near-infrared pulses of relatively low intensity, the intensity dependence of the electronic excitation energy exhibits perturbative trends due to multiphoton absorption process. Tunnel ionization of electrons is the relevant photoionization mechanism induced by strong few-cycle, mid-infrared pulses. For Si irradiated by mid-infrared laser pulse, we find that there is a laser intensity threshold below which no energy is absorbed inside the bulk; no such response is found for Ge. In the high laser intensity regime, we find intensity thresholds above which the absorbed energy per atom becomes independent of the laser

wavelength. In this regime, the electronic excitation energies exceed the melting temperatures in Si and Ge, which is a prerequisite for nonthermal melting of the materials. Below the bulk damage threshold, the results may provide valuable information for ultrafast changes of optical constants of silicon and germanium at near- and mid-infrared frequencies. Above the estimated dielectric breakdown thresholds, our numerical results may be helpful in finding a regime of laser parameters relevant for the nonthermal laser processing of silicon and germanium. In a follow up paper we intend to present results on the detailed microscopic response of electrons in these materials, including the transient density distributions and interband coherences.

ACKNOWLEDGMENT

This work is supported by the Bulgarian National Science Fund under Contracts No. DNTS/France-01/9, No.DN-18/7 and No.DN-18/11 (T.A.) and by the Bulgarian National Science Fund under Contract No. 08-17 (B.O.).

REFERENCES

- [1] G. Wachter, C. Lemell, J. Burgdorfer, S. A. Sato, X. Tong, and K. Yabana, "Ab Initio Simulation of Electrical Currents Induced by Ultrafast Laser Excitation of Dielectric Materials", *Phys. Rev. Lett.*, vol. 113, pp. 087401-087406, 2014, doi:10.1103/PhysRevLett.113.087401.61.2643
- [2] A. Schiffrin, T. Paasch-Colberg, N. Karpowicz, V. Apalkov, D. Gerster, S. Muhlbrandt, et al., *Nature* vol. 493, pp. 70-74, 2013, doi: 10.1038/nature11567
- [3] A. Rousse, C. Rischel, S. Fourmaux, I. Uschmann, S. Sebban, G. Grillon, P. Balcou, et al., "Non-thermal melting in semiconductors measured at femtosecond resolution", *Nature*, vol. 410, pp. 65-68, 2001
- [4] K. Sokolowski-Tinten and D. von der Linde, "Generation of dense electron-hole plasmas in silicon", *Phys. Rev. B* vol. 61, pp. 2643-2650, 2000, doi:10.1103/PhysRevB.61.2643
- [5] J. Bonse, G. Bachelier, J. Siegel, and J. Solis, "Time- and space-resolved dynamics of melting, ablation, and solidification phenomena induced by femtosecond laser pulses in germanium", *Physical Review B*, vol. 74, pp. 134106-134119, 2006, doi: 10.1103/PhysRevB.74.134106
- [6] J. Forneris, S. Ditalia Tchernij, P. Traina, E. Moreva, N. Skukan, M. Jakširc, et al., "Mapping the Local Spatial Charge in Defective Diamond by Means of N-V Sensors—A Self-Diagnostic Concept", *Physical Review Applied* vol. 10, pp. 014024-014039, 2018
- [7] S. Lagomarsino, M. Bellini, C. Corsi, S. Fanetti, F. Gorelli, Liontos, G. Parrini, et al., "Electrical and Raman-imaging characterization of laser-made electrodes for 3D diamond detectors", *Diamond Relat. Mater.* vol. 43, pp. 23-28, 2014, doi:10.1016/j.diamond.2014.01.002
- [8] A. Boltasseva and H. A. Atwater, *Science* vol. 331, pp. 290-291, 2011, doi: 10.1126/science.1198258
- [9] I. Staude and J. Schilling, "Metamaterial-inspired silicon nanophotonics", *Nature Photonics*, vol. 11, pp. 274-284, 2017
- [10] B. Obreshkov and T. Apostolova, "Photoionization of Diamond Interacting with Intense 30fs Laser Pulse", *Bulg. J. Phys.* vol. 42, pp. 305-314, 2015
- [11] S. Lagomarsino, S. Sciortino, B. Obreshkov, T. Apostolova, C. Corsi, M. Bellini, et al., "Photoionization of monocrystalline CVD diamond irradiated with ultrashort intense laser pulse", *Phys. Rev. B*, vol. 93, pp. 085128-085139, 2016, doi: 10.1103/PhysRevB.93.085128

- [12] T. Apostolova, B. Obreshkov, Ionin A.A., Kudryashov S.I., Makarov S.V., Mel'nik N.N., et al., "Ultrafast photoionization and excitation of surface-plasmon-polaritons on diamond surfaces", *Applied Surface Science*, vol. 427, pp. 334-343, 2018, doi:10.1016/j.apsusc.2017.07.263
- [13] T. Apostolova and B. Obreshkov, "High harmonic Generation from Bulk Diamond driven by Intense femtosecond laser pulse", *Diamond and Related Materials*, vol. 82, pp. 165-172, 2018, doi: 10.1016/j.diamond.2017.12.013
- [14] M. L. Cohen and T. K. Bergstresser, *Phys. Rev.* vol. 141, pp. 789-796, 1966
- [15] S. A. Sato, K. Yabana, Y. Shinohara, T. Otobe, and G. F. Bertsch, "Numerical pump-probe experiments of laser-excited silicon in nonequilibrium phase", *Phys. Rev. B*, vol. 89, pp. 064304- 064312, 2014, doi: 10.1103/PhysRevB.89.064304
- [16] C. C. Yang and Q. Jiang, "Effect of pressure on melting temperature of silicon and germanium", *Materials Science Forum*, Vols. 475-479 (2005), pp. 1893-1896, doi:10.4028/www.scientific.net/MSF.475-479.1893